INFLUENCE OF STATIONARY COMPONENTS ON UNSTEADY FLOW IN INDUSTRIAL CENTRIFUGAL COMPRESSORS

Luciano Bonciani and Luciano Terrinoni
Nuovo Pignone
Florence, Italy

An experimental investigation was performed to determine the characteristics of the onset and the growth of rotating nonuniform flow in a standard low specific speed stage, normally utilized in high pressure applications, in relation to change of stationary component geometry.
Four configurations, differing only in the return channel and crossover geometry were tested on an atmospheric pressure open loop test rig.
Experimental results make conspicuous the effect of return channel geometry and give the possibility of shifting the unstable zone onset varying such geometry.
An attempt was made to interpret the experimental results in the light of Emmons - Stenning's rotating stall theory.

1. INTRODUCTION.

Present experience with aeroinduced vibrations in turbomachines has emphasized two types of aerodynamic forces giving rise to completely different kinds of vibrational behavior:

- Forces depending on displacement and displacement velocity of the rotor

- Forces independent of rotor vibration caused by aerodynamic instability of the flow somewhere in the machine.

Although such forces are always present, usually they do not pose operational problems in low density applications. However, when the gas handled density increases, their intensity can grow till causing severe vibration problems.
Forces of the first type can completely destroy the damping present in the system, giving rise to high amplitude limit cycles at the first natural bending frequency of the rotor (often, unfortunately, the limit cycle amplitude is higher than the allowable clearances) (Ref. 1-8).
Forces of the second type are more benevolent in nature: their effect is limited to a strong low frequency vibration of the rotor.
In this case, the frequency, in a figurative sense, belongs to the force not to the rotor and the amplitude depends on the damping and stiffness characteristics of the rotor-bearing system (which are unaffected by the phenomenon).

Full load tests carried out on centrifugal compressors (Ref. 9, 10, 11) have put in evidence that forces of the second type always arise near the surge when reducing the flow at constant speed.
It is quite remarkable that the second type phenomenon can easily be studied even at atmospheric pressure (Ref. 21).
In order to provide a deeper understanding of the phenomenon, a research program was scheduled with the following main aims:

- Identifying the parameters ruling the unsteady flow condition onset.

- Finding, if possible, which of the stage components (impeller, diffuser, return channel) bears major responsibility.

- Defining the modifications necessary to displace the phenomenon onset (can it happen near an operating point? And if so, what should be done?).

This paper describes the results of such research, obtained studying a typical reinjection stage, tested in four configurations. Part of the results have already been presented (Ref. 21).

SYMBOLS

R	Radius (m)
P	Static pressure (kgf/m^2)
Po	Total pressure (kgf/m^2)
q	Dynamic pressure (kgf/m^2)
Ω	Impeller angular speed (sec^{-1})
Cr	Radial velocity (m/sec.)
C_ϑ	Tangential velocity (m/sec.)
f_s	Fundamental frequency of pressure oscillations (sec^{-1})
A	Amplitude of pressure oscillations (kgf/m^2)
$\hat{C}r$	Nondimensional radial velocity ($\hat{C}r = Cr/\Omega R$)
$\hat{C}_\vartheta$	Nondimensional tangential velocity ($\hat{C}_\vartheta = C_\vartheta / \Omega R$)
$\hat{f}_s$	Fundamental frequency of pressure oscillations normalized to impeller speed ($\hat{f}_s = 2\pi f_s / \Omega$)

$\hat{A}$ Amplitude of pressure oscillations nondimensionalized with dynamic pressure ($\hat{A} = A/q$)

Mu Tip speed Mach number

φ Inlet flow coefficient

τ Total enthalpy rise coefficient

α Absolute flow angle (referring to tangential direction) (Deg.)

β_5 Inlet angle of return channel vanes (referring to tangential direction) (Deg.)

i_5 Incidence angle on return channel vanes ($i_5 = \alpha_5 - \beta_5$) (Deg.)

Cp Pressure recovery coefficient

Subscripts:

10 = Measured at section 10

10' = " " " 10'

20 = " " " 20

20' = " " " 20'

30 = " " " 30'

40 = " " " 40

40' = " " " 40'

50' = " " " 50'

60 = " " " 60

60' = " " " 60'

D = Diffuser

RC = Return channel

* = Onset of unsteady flow

2. TEST FACILITIES AND INSTRUMENTATION.

Tests were performed on an atmospheric pressure open loop test rig dedicated to the individual stage development (Ref. 12). A cross section of the test rig is shown in Fig. 1. The stage consisted of an impeller, a free-vortex diffuser, a crossover and a return channel.
Speed was adjusted by an hydraulic coupling torque converter while an electrically actuated discharge valve was operated to vary the flow.
Table 1 shows the conventional instrumentation usually used for industrial stage development testing.
Table 2 shows the instrumentation utilized to detect pressure oscillations connected with nonstationary flow conditions. Details of the conventional instrumentation are given below.

- The data acquisition system was based on a Solartron system 35 with a PDP 11/03 control unit.
- All pressure readings were connected, through a scannivalve, to a single pressure transducer. The transfer function of the measurement chain was experimentally tested to check that the output was the time average of the pressure within the frequency range of interest.

Regarding nonstationary readings we can note that:

- Static pressure probes were the Kulite XT-190-50 type
- Dynamic pressure probes were the Kulite XB-093-50G type
- Probe signals were recorded on an Ampex PR 2200 tape recorder and finally analyzed through an Ono-Sokki CF-500 real time spectrum analyzer. Data shown for each tested point are the RMS average of 256 spectra.

Four configurations (indicated in the following by the capital letters A, B, C, D) were tested, differing only in return channel and crossover geometry. The main geometrical dimensions are shown in Table 3.

3. DATA REDUCTION.

A brief note about data reduction may be in order here.

- At every measurement section, along the flow path in the stage, static pressure is assumed to be the average of the readings from the available pressure taps.
- The inlet and outlet stage values of the total pressure (sections 10 and 60) are the average of the readings from a four-Kiel type probe rack.
- Total pressure and flow angle traverse data at diffuser inlet and outlet (sections 20 and 40) were taken using a three-hole Cobra probe. Such readings were combined with the static pressure value and the total temperature readings, in order to calculate a mass-averaged total pressure.
- Total inlet temperature was assumed to be the average of the readings from eight circumferentially and radially spaced thermocouples.
- Total temperature traverse data at section 20 were taken with two thermocouples. Such values were combined with total and static pressure values in order to calculate a mass-averaged total temperature.

- Total temperature at section 40 was not measured: the mass-averaged value calculated from section 20 was assumed valid for section 40 too.
- Total outlet temperature (section 60) was practically coincident with the one measured at section 20 (except for efficiency calculation purposes), thus confirming the validity of the previous assumption.
- Flow angles were measured by Cobra probes at sections 10, 20, 40.

Measured angles at sections 20 and 40 showed a regular trend with the flow in the steady flow zone, but were found badly scattered in the unsteady one. On the contrary the angles calculated using

. Mass-flow
. Static pressure
. Mass-averaged total pressure
. Mass-averaged total temperature

showed a regular trend with flow under any condition (steady or unsteady). They were found to be strictly repetitive and were in good agreement, in the steady flow region, with the angles measured by the Cobras at the middle of the diffuser width.

At section 20 an additional check was performed calculating the angle by

. Mass-flow
. Static pressure
. Mass-averaged total temperature rise.

The agreement between the two procedures was satisfactory. As the latter method could be applied only to section 20, the former one was chosen for both sections.

Finally a very important parameter, the incidence angle on the return channel leading edge i_5, was calculated from the continuity equation assuming constant density and angular momentum conservation between station 40 and return channel inlet.

4. TEST PROCEDURE DESCRIPTION.

Each configuration was tested by varying the flow from the maximum allowed till surge and vice versa at constant speed. The procedure was then repeated at different speeds.
While testing configuration A the readings from the conventional instrumentation were not recorded simultaneously with the pressure oscillation readings (see Ref. 21); during other configuration tests, time-averaged and instantaneous measurements were recorded together.

5. TEST RESULTS.

5.1. Configuration A.

5.1.1. Unsteady flow behavior.

The test results (detailed in Ref. 21) will be, for the sake of completeness,

briefly summarized here.
Fig. 2 shows the observed frequencies normalized to the impeller angular speed versus the inlet flow coefficient. Reducing the flow at constant speed, the following behavior was observed:

. Pressure oscillations started simultaneously on all pressure transducers with very low amplitude and almost sinusoidal shape.
. A small flow reduction resulted in a slight increase in frequency and a considerable increase in amplitude, the signal shape remaining sinusoidal.
. Further flow reductions produced different results according to the test tip speed Mach number. It was found that the unsteady flow pattern could exhibit two distinct shapes:
  - A double frequency shape (DFS) so indicated because the frequency analysis showed the presence of two components at f_s and $f_s/2$ having practically the same amplitude.
  - A single frequency shape (SFS) characterized by a dominant component at f_s. Higher order harmonics, while present in both cases, had negligible amplitudes.

  The phase difference between static probes at the same radius was 90° for the DFS signal and 180° for the SFS one, thus indicating that DFS was associated with a single lobe pattern while SFS was associated with a two lobe one. It was found that at Mu = 0.45 and Mu = 0.60, the DFS was stable from the onset region till the region before surge, where a sudden shift to the SFS shape was always found. At higher test Mach numbers (Mu = 0.75 and Mu = 0.85) the switch from one shape to the other could happen in practically any point of the unsteady flow region, but the factors governing it were not understood: sometimes a spontaneous transition from the SFS to the DFS was observed several minutes after the latest valve positioning, sometimes (but not always) the introduction of the conventional probes into the diffuser was able to trigger such transition.
. Amplitudes at section 10' (impeller inlet) were always negligible till the surge.
. On opening the valve and exploring the phenomenon starting from the surge, the frequencies and amplitudes were generally repetitive related to flow; however, a slight hysteresis was noted in the onset region.

Since it was evident from the test results that two different unsteady patterns were fully compatible with the same flow and RPM (or better with the same φ - Mu values), an attempt to stabilize one of the two patterns was made. To attain this aim a small strip of sandpaper was glued on the leading edge (suction side) of five consecutive vanes of the return channel.

Testing such configuration, no difference was found in the onset zone, but the DFS was not found anymore at whatever test Mach number. In addition, the single frequency shape exhibited the same amplitude, frequency and phase lag than before for a given flow coefficient and tip speed Mach number (Fig. 3). After this result, no additional tests were carried out on configuration A.

5.1.2. Time-averaged results.

Fig. 4 shows the pressure ratios at section 60 (static-to-total and total-to-total) versus flow coefficient. A variation in the slope can be noted at the onset of the pressure oscillations followed by a region with a positive slope. At Mu = 0.75 and Mu = 0.85, two distinct branches clearly identify the regions relevant to the two shapes of the previously described signal (DFS and SFS). The inlet flow coefficient corresponding to the onset of the pressure oscillations continuously grows when the tip speed Mach number increases. However, if the inlet flow coefficient is plotted versus any of the impeller outlet variables, for example $\hat{C}_{r20}$ as shown on Fig. 5, it can be noted that the unsteady flow condition invariably appears for a practically constant value of such variables. In addition, as the more interesting parameters are surely the flow angles, we can note that the onset values are (see Fig. 6):

$$\alpha_{20*} \simeq 10°$$

$$\alpha_{40*} \simeq 13°$$

$$i_{5*} \simeq -6°$$

The behavior of the diffuser pressure recovery coefficient (Fig. 7) shows considerable scattering corresponding to the α_{20} onset value.
Quite remarkable is the sudden drop of the return channel pressure recovery coefficient C_{pRC} (Fig. 8) corresponding to the i_5 onset value. The figure clearly shows the two branches corresponding to the two signal shapes shown before.
Figs. 9, 10, 11, 12, 13 show the behavior of the configuration A with sandpaper on the return channel vanes. While the unsteady flow onset values (i_5 in particular) are unchanged, the return channel pressure recovery coefficient presents only the lower branch (SFS) to the left of the onset discontinuitv.
The following tendency in readings at sections 20 and 40 in the unsteady flow region is worth noting:

- While total temperature readings at section 20 did not show any trend to flatten after the onset (Fig. 14), total pressure readings, on the contrary, tended to flatten and even to decrease, so that dynamic pressure at section 20 tended to decrease too (Fig. 15).
  The agreement between the measured total pressure and the one calculated from total temperature rise, static pressure and mass flow got poorer and poorer. Even higher deviations from a regular trend are found at section 40 (Fig. 15). Measured flow angles began to be badly scattered, previous agreement with the calculated values being gradually lost.

This behavior of the readings was almost the same for every configuration tested.

5.2. Configuration B.

Configuration B differs from configuration A only in the return channel width and the crossover geometry as reported in Ref. 21. The width was increased to have, at the design point of the stage, an incidence angle on the R.C. leading edge, equal to - 6 degrees (the onset value for the configuration A).

5.2.1. Unsteady flow behavior.

This time only the single frequency shape was encountered all over the tested range of tip speed Mach numbers. The onset as well as the growth of the pressure oscillations was found to be quite similar to the one experienced when testing the configuration A when the SFS was present. Fig. 16 shows the observed frequencies, normalized to the impeller angular speed, versus the inlet flow coefficient.
The phase difference between static probes at the same radius was 180° as observed for the SFS signal in the previous configuration.

5.2.2. Time-averaged results.

The onset of the unsteady flow (Fig. 17) was now shifted to considerably higher flows. As before, the onset of the pressure oscillations started for a constant value of any impeller exit variable (Fig. 18). However, in this case, we found (see Fig. 19):

$$\alpha_{20*} \simeq 14°$$

$$\alpha_{40*} \simeq 18°$$

$$i_{5*} \simeq -6°$$

As the calculated R.C. incidence angle is practically coincident with the critical one found when testing configuration A, while vaneless diffuser inlet angles differ 4 degrees, it seems evident that the phenomenon tracks the return channel.
As before, the R.C. pressure recovery coefficient exhibited a sudden drop, coinciding with the start of the pressure oscillations, but only the lower branch to the left of the onset discontinuity was observed (Fig. 20).
Fig. 21 shows the diffuser pressure recovery coefficient versus α_{20}. Scattering is reduced and the onset drop is less evident.

5.3. Configuration C.

In order to obtain additional confirmation of the previous test results, a different channel was designed, having the same width of the B one but a lower vane inlet angle. The modified vane had a greater camberline curvature and a slightly different thickness distribution on the leading edge zone. The aim was to displace the onset back to the zone where it was found when testing the configuration A.

5.3.1. Unsteady flow behavior.

Only the test at Mu = 0.75 has been analyzed in detail, as behavior at different tip speed Much numbers was similar. Again, the onset and the growth of the pressure oscillations was found to be very similar to the ones previously shown. The signal corresponding to unsteady flow was once more a single frequency shape (Fig. 22) with 180° phase lag.

5.3.2. Time-averaged results.

As can be seen, the onset was now displaced to a slightly lower value, but higher than the expected one (Figs. 23 and 24). The diffuser inlet and exit flow angle at the onset were (see Fig. 25):

$$\alpha_{20*} \simeq 13°$$

$$\alpha_{40*} \simeq 16°$$

As before, the onset of pressure oscillations coincides with a sudden drop of the return channel pressure recovery coefficient (Fig. 26). The same figure suggests the reason for the apparent failure: the new return channel exhibits a lower critical incidence. The camberline modification seems to have lowered the critical incidence angle from - 6 to - 4 degrees. Therefore, the onset flow coefficient is about 20% higher than expected based on $i_5 = -6°$.

5.4. Configuration D.

At this point, an additional verification was of course necessary: the return channel width was reduced, keeping unchanged the camberline and the thickness distribution. The width was chosen equal to configuration A 's to facilitate the comparison.

5.4.1. Unsteady flow behavior.

The general behavior, from the point of view of the onset and the growth of the phenomenon, was essentially unchanged.
The present configuration resembled the configuration A: the double frequency shape was again encountered at both tested tip speed Mach numbers (Fig. 28).
In addition at Mu = 0.45 a certain sensitivity to the introduction of the pressure probes in the diffuser was found. In this case, however, the effect was not the shift from SFS to DFS signal but a slight frequency variation of SFS. Such sensitivity was not noted at Mu = 0.75.
The phase lag was 180° for SFS and again 90° for the DFS signal.

5.4.2. Time-averaged results.

Figs. 29, 30, 31 show that the unsteady region was displaced to a lower flow coefficient and the diffuser inlet and exit flow angle at the onset were

$\alpha_{20*} \simeq 9°$

$\alpha_{40*} \simeq 11°5$

Again the return channel pressure recovery coefficient (Fig. 32) shows a discontinuity corresponding to the pressure oscillation start.
The hypothesis of a lower critical incidence angle due to the camberline and thickness modification seems to be confirmed: the incidence angle at R.C. leading edge on the onset was again $i_{5*} \simeq -4°$.
Finally, Fig. 33 shows the behavior of the diffuser Cp_D.

6. NONDIMENSIONAL FREQUENCY AND AMPLITUDE OF THE PRESSURE OSCILLATIONS.

The analysis of the experimental results easily suggests that, for each configuration, the frequency-amplitude curves at different Mach numbers can be made to collapse, with a suitable choice of nondimensionalization factors, when plotted versus whatever outlet variable. The choice of the scale factors and of the outlet variable can be made in many ways, bringing in all cases to a single curve for the frequency and for the pressure amplitude. However, the four tested configurations differ only in the R.C. geometry and, in every case, the onset of the unsteady flow was found to correspond to a constant value of the incidence on the leading edge of the R.C. vanes. The phenomenon seems to be controlled by the R.C. to such a large extent that five strips of sandpaper were sufficient, when testing configuration A, to eliminate the double frequency shape. Such considerations suggest as the best nondimensionalization factor for the frequency the angular speed at section 40 ($C_{\vartheta 40}/R_{40}$).
As for the amplitudes, it was found that, using the local dynamic pressure as nondimensionalization factor, the same order of magnitude was obtained at every measurement section (with the exception of the impeller inlet). So in the following, the four configuration results will be compared on the basis of the so defined nondimensional frequency and amplitude (at section 40') versus R.C. vane incidence angle.

6.1. Comparison of the nondimensional frequency and amplitudes for the A, B, C, D, configurations.

The data reduction results are shown in Figs. 34, 35, 36 (configuration A), Figs. 37, 38 (configuration A with sandpaper), Figs. 39, 40 (configuration B), Figs. 41, 42 (configuration C) and finally in Figs. 43, 44, 45 (for configuration D). In any case the reduction to a single curve is very satisfactory.
Comparing all the nondimensional frequency plots we can note:

- The nondimensional frequency, $f_s/C_{\vartheta_{40}}$, is practically a linear function of the incidence and the slope is almost the same for each configuration.
- The onset values of the nondimensional frequency (both SFS and DFS when present) are the same for configurations having the same inlet width.
- Nondimensional amplitude curves (A_{40}/q_{40}) of configurations A and B are practically coincident. The corresponding curve of configuration C can be made to coincide with the preceding ones by an incidence shift of 2 degrees. Configuration D seems to be a case somewhat apart: the amplitudes are comparatively lower and very scattered.

So, the comparison seems to lead to the following conclusion:
- The frequency curves can be represented fairly accurately by

$$\hat{f}_s/\hat{C}_{\vartheta_{40}} = (\hat{f}_s/\hat{C}_{\vartheta_{40}})_* + K(i_5 - i_{5*})$$

but while the K value is the same for each configuration, $(\hat{f}_s/\hat{C}_{\vartheta_{40}})_*$ seems to depend on the relative width of the return channel.
For configurations A and D, we have:

$K \simeq 0.057$ (i_5 measured in degrees)

$(\hat{f}_s/\hat{C}_{\vartheta_{40}})_* \simeq 0.25\text{-}0.30$

Exactly half of such values is of course found for $f_s/2$ when the DFS is present.
For configurations B and C, we have:

$K \simeq 0.057$

$(\hat{f}_s/\hat{C}_{\vartheta_{40}})_* \simeq 0.18\text{-}0.22$

- The amplitude curves can be represented fairly well by a single relation of the kind

$$\hat{A} = f(i_5 - i_{5*})$$

for configurations A, B, C. No explanation can be suggested for the apparent deviation of configuration D.

It is a bit puzzling that the relative width of the return channel seems to influence only the onset values of nondimensional frequency, but not the slope of the frequency versus incidence curves, nor the amplitude relations (at least for configurations A, B, C).

7. AN APPLICATION OF ROTATING STALL THEORIES.

In the light of the previous discussion, it seems that the phenomenon can be explained on the basis of rotating stall on the R.C. vanes.

So an attempt can be made to utilize the existing theories on rotating stall. Due to the complexity of the problem, most of such theories (Ref. 22, 23, 24, 25) are based on an inviscid, linearized formulation of the motion equations. This approach is able to give information about the stall propagation speed as a function of some steady-state parameters (speed, inlet angle, pressure rise coefficient etc.). As natural consequence of the linearization, the pressure oscillation amplitudes and the spatial stall configuration are left indetermined. Even though the agreement with the experimental results is only fair, such methods are useful in providing qualitative understanding of the phenomena and in suggesting correlations among the relevant parameters.

7.1. Emmons - Stenning's theory.

Emmons - Stenning's theory is a typical flow stability calculation which can be extended without difficulties to cascades between revolution surfaces. Basic assumptions are:

- The flow upstream the cascade is potential and the fluctuating velocity components vanish at infinity.
- The cascade pressure rise coefficient derived from steady conditions is considered valid in unsteady conditions too.
- Pressure oscillations at the cascade outlet are negligible.

The calculated stall speed is then given by

$$\frac{Vp}{C_\vartheta} = \frac{1}{1+nJ} \cdot \frac{1 - Cp}{\cos^2\alpha}$$

where n is the number of lobes and J a geometrical nondimensional parameter (see appendix A). As a consequence, the (calculated) observed frequencies are given by

$$\frac{\omega_s R}{C_\vartheta} = \frac{n}{1+nJ} \cdot \frac{1-Cp}{\cos^2\alpha} = \frac{\hat{f}_s}{\hat{C}_\vartheta}$$

Some criticism can of course be made about the use of such relations in the present case:

- The pressure oscillations do not fade away with the distance from the leading edge of the R.C. vanes, showing that the coupling with the impeller-diffuser system cannot be neglected.
- Due to the influence of the impeller outlet fluctuating conditions, the flow in the diffuser can hardly be considered potential in nature.

A more complete analysis could be attempted which, while retaining the basic hypotheses of the previous theory, takes into account the interference between the return channel and the other components of the stage.
However, an attempt to find a correlation with the variables involved in the Emmons and Stenning's formula is justified by the strong influence of the R.C. geometry on the phenomenon.

To this end, the observed nondimensional frequencies were plotted versus $(1-C_{pRC})/\cos^2\alpha_5$ with the exclusion of configuration A (the lack of simultaneousness between conventional measurement and pressure oscillation readings hindered that).

Comparing all the nondimensional frequencies versus $(1-Cp_{RC})/\cos^2\alpha_5$ plots (Figs. 46, 47, 48, 49) we can note:

- For each configuration there exists a range of the abscissa values where the curve is practically linear. This range corresponds to the narrow range of flow where the Cp_{RC} suddenly drops, just after the onset. In this zone (the only zone where the theory can be expected to work), the agreement between theoretical and experimental results is fairly good. When the pressure oscillation amplitude increases, the linear relation is lost and the frequency becomes quite independent of the abscissa.
- Configurations having the same R.C. width exhibit almost identical curves. However, the slope of the linear zone is different for configurations A, D and configurations B, C. While the theory accounts for geometrical differences through the J factor, the slope difference is higher than predicted.
- The agreement between theoretical and experimental results is better for configurations A and D. Such condition is however limited to the upper frequency in case of DFS signal: the lower one is overestimated. It is worthy of note that in such case the ratio of the predicted frequencies is not integer, while during the configuration A, D tests such ratio was exactly 2.

In view of the limits of the present approach, expecting such details from the theory appears to be asking a bit much. On the whole, the results can be considered fairly satisfactory. It must be remarked that the Emmons-Stenning's theory provides a correlation rather than a prediction method: critical incidence, maximum Cp etc. cannot usually be predicted with the required accuracy.

8. CONCLUSIONS.

The main results of the present investigation are the following:

1. The four configurations clearly showed that the return channel bears major responsibility for the onset of the unsteady flow.
2. For every configuration, the unsteady flow onset was found to occur when a well defined incidence angle on the leading edge of the return channel vanes was reached. The critical incidence was found to be dependent on the vane skeleton, but independent of the crossover geometry.
3. The general behavior of the nondimensional frequencies and amplitudes is similar for the four configurations when plotted versus the difference between the actual incidence and the critical one. However, the narrower return channels exhibited higher onset frequencies and, in addition, could exhibit two distinct unsteady flow patterns (SFS and DFS). Within the tested Mu range, such behavior was never observed with the wider ones (configurations B and C).
4. The comparison with the Emmons-Stenning's theory can be considered fairly satisfactory and provides additional confirmation of the fact that the phenomenon is controlled by the return channel rotating stall.

Additional theoretical and experimental work would be required in order to complete and extend the present results.

REFERENCES

1. Fowlie D.W., Miles D.D., Vibration Problems with High Pressure Centrifugal Compressors, ASME Paper n. 75-Pet-28

2. Smith K.J., An Operation History of Fractional Frequency Whirl, Proc. 4th Turbomachinery Symposium, Gas Turbine Laboratories, Texas A & M University, Oct 1975.

3. Wachel J.C., Nonsynchronous Instability of Centrifugal Compressors, ASME Paper n. 75-Pet-22.

4. Criqui A.F., Wendt P.G., Design and Closed Loop Testing of High Pressure Centrifugal Gas Compressors for the Suppression of Subsynchronous Vibrations, ASME Paper n. 79-GT-86.

5. Fujikawa T., Ishiguaro N., Ito M., Asynchronous Vibration Problem of Centrifugal Compressor, NASA Conference Publication 2133, May 12-14, 1980.

6. Coletti N.J., Crane M.E., Centrifugal Compression of the Arun High Pressure Injection Project, I. Mech. E. 1981, C 54/81.

7. Wachel J.C., Rotordynamic Instability Field Problems, NASA Conference Publication 3250, May 10-12, 1982

8. EK. M.C., Solution of the Subsynchronous Whirl Problem in the High Pressure Hydrogen Turbomachinery of the Space Shuttle Main Engine, AIAA/SAE 14th Joint Propulsion Conference, Las Vegas, Nevada, July 25-27, 1978.

9. Ferrara P.L., Tesei A., High Pressure Centrifugal Compressors, Inst. Mech. Eng. Conference Publications 1978, March 3, 1978.

10. Bonciani L., Ferrara P.L., Timori A., Aero-Induced Vibrations in Centrifugal Compressors, NASA Conference Publication 2133, May 12-14, 1980.

11. Sabella D., Terrinoni L., Timori A., Full Load Testing of Centrifugal Natural Gas Injection Compressors, Inst. Mech. Eng. Conference Publication 1981, March 3, 1981.

12. Benvenuti E., Aerodynamic Development of Stages for Industrial Centrifugal Compressors, Part. 1 & 2, ASME Paper n. 8-GT 4 & 5.

13. Jansen W., Rotating Stall in a Radial Vaneless Diffuser, Transaction of the ASME Journal of Basic Engineering, Dec. 1964 pp. 750-758.

14. Abdelhamid A.N., Colwill W.H., Barrows J.F., Experimental Investigation of Unsteady Flow Phenomena in Vaneless Radial Diffusers, ASME Paper n. 78-GT-23.

15. Abdelhamid A.N., Bertrand J., Distinctions Between Two Types of Selfexcited Gas Oscillations in Vaneless Radial Diffusers, ASME Paper n. 79-GT-58.

16. Abdelhamid A.N., Analysis of Rotating Stall in Vaneless Diffusers of Centrifugal Compressors, ASME Paper n. 80-GT-184.

17. Abdelhamid A.N., Effects of Vaneless Diffuser Geometry on Flow Instability in Centrifugal Compression Systems, ASME Paper n. 81-GT-10.

18. Abdelhamid A.N., Control of Selfexited Flow Oscillations in Vaneless Diffuser of Centrifugal Compressor Systems, ASME Paper n. 82-GT-188.

19. Van Den Braembussche R., Frigne P., Roustan M., Rotating Nonuniform Flow in Radial Compressors, AGARD C.P. 282, May 1980.

20. Van Den Braembussche R., Frigne P. Comparative Study of Subsynchronous Rotating Flow Patterns in Centrifugal Compressors with Vaneless Diffusers, NASA Conference Publication 2250, May 10-12, 1982.

21. Bonciani L., Terrinoni L., Tesei A., Unsteady Flow Phenomena in Industrial Centrifugal Compressor Stage, NASA Conference Publication 2250, May 10-12, 1982.

22. Emmons H.W., Pearson C.E., Grant N.P., Compressors Surge and Stall Propagation, Trans. ASME Vol. 77, 1955.

23. Stenning A.H., Kriebel A.R., Stall Propagation in a Cascade of Aerofoils, ASME Paper n. 57-SA-29.

24. Leone M.J., A Study of Existing Information on Rotating Stall with New Observations Concerning Changes in Stall-cell Size and Number, Rensselaer Polytechnic Inst., TR. A.E. 6810, September 1968.

25. Ludwig G.R., Nenni J.P., Rice J.R.R.S., An Investigation of Rotating Stall Phenomena, Cornell Aeronautical Laboratory, Inc. Buffalo, N.Y. - TR AFAPT-TR-70-26, May 1970.

APPENDIX A

STABILITY OF THE FLOW THROUGH AN ISOLATED CASCADE.

A brief account of the Emmons-Stenning's theory will be given here.
Suppose we have an isolated annular cascade bounded by revolution surfaces extended, upstream and downstream at a great distance compared with the blade meridional length. The motion equations (with the assumptions below specified) are written for the upstream field and the flow between the blades (a major assumption of the theory makes calculations for the downstream field unnecessary) and a stability analysis is performed in a classical way.

1. Upstream field.
   Assuming incompressible nonviscous flow with uniform conditions at infinity, the energy equation in a system rotating with the cascade is written

$$\frac{\partial \phi}{\partial t} + \frac{p}{\rho} + \frac{\omega^2}{2} - \frac{U^2}{2} = \frac{p_0}{\rho}$$

   where ϕ, ω, U are the velocity potential, the relative flow velocity and the local blade velocity ($U = \Omega r$), while p_0 is the stagnation pressure.

2. Cascade.
   Assuming incompressible unidimensional flow, the motion equation is written

$$\frac{\partial w}{\partial t} + w\frac{\partial w}{\partial l} - U\frac{\partial U}{\partial l} = -\frac{1}{\rho}\frac{\partial p}{\partial l} - \frac{f}{\rho}$$

   where w, U have the usual meaning and f is the term due to the wall shear stresses.
   Integrating along the mean line of the channel from the inlet (1) to the outlet (2), we obtain

1. $$\int_0^L \frac{\partial w}{\partial t}\,dl + \frac{w_2^2 - w_1^2}{2} + \int_0^L \frac{f}{\rho}\,dl - \frac{U_2^2 - U_1^2}{2} + \frac{p_2 - p_1}{\rho} = 0$$

   The following procedure is now followed:
   - Each equation is linearized using as reference the steady conditions and retaining the first order terms only. Due to the assumed conditions, the upstream perturbation field is potential and the velocity is given by

$$w_m = W_m + \frac{\partial \phi}{\partial m}$$

$$w_\theta = W_\theta + \frac{\partial \phi}{r\,\partial \theta}$$

- Upstream perturbation velocity variation along the cascade pitch is negligible. This immediately allows expressing the velocity perturbation between the blades as

$$w = \frac{s\,b_1}{A}\,\frac{\partial \phi}{\partial m}$$

where s, b_1, A are the pitch, the inlet width and the normal section of the channel defined by two consecutive blades.

- When linearizing equation 1, it is assumed that the term

$$\frac{w_1^2 - w_2^2}{2} - \int_0^L \frac{f}{\rho}\,dl$$

can be represented, even in unsteady conditions, by

$$C_p\,(tg\beta_1)\,\frac{1}{2}\,(w_{m_1}^2 + w_{\theta_1}^2)$$

where β_1, w_{m_1}, w_{θ_1} are the flow angle and the velocity components at the cascade inlet.

- Lastly, outlet pressure variations are assumed to be zero all over the circumference. This assumption, suggested by the physical behavior of a cascade in incipient stall, allows a major simplification: we no longer have to calculate the downstream field which, never being potential in unsteady conditions, usually poses greater difficulties than the upstream. Eliminating the inlet pressure variations, we finally find

$$\frac{\partial \phi}{\partial t} + \left(b_1 s \int_0^L \frac{dl}{A}\right) \frac{\partial^2 \phi}{\partial m \partial t} +$$

$$\left\{(1 - C_p)\,W_{m_1} - \frac{\partial C_p}{\partial\, tg\beta_1}\, tg\beta_1 \frac{w_1^2}{2 W_{m_1}}\right\} \frac{\partial \phi}{\partial m} +$$

$$\left\{(1 - C_p)\,W_{\theta_1} + \frac{\partial C_p}{\partial\, tg\beta_1}\, tg\beta_1 \frac{w_1^2}{2 W_{\theta_1}}\right\} \frac{\partial \phi}{r\,\partial \theta} = 0$$

where the perturbation potential derivatives have to be calculated at the cascade inlet (m = 0).

The potential ϕ must satisfy the equation

$$\frac{\partial}{\partial m}\left(br\frac{\partial \phi}{\partial m}\right) + \frac{b}{r^2}\frac{\partial^2 \phi}{\partial \theta^2} = 0$$

with the condition

$$\lim_{m \to -\infty} \nabla \phi = 0$$

It is convenient to perform a change of variable by defining

$$\xi = \int_0^m \frac{dm}{r}$$

and to develop the potential in Fourier series

$$\phi = \Sigma A X_n(\xi) e^{in\theta}$$

where the functions X_n are the solutions of the boundary value problem

$$\frac{d^2 X_n}{d\xi^2} + \frac{1}{b}\frac{db}{d\xi}\frac{dX_n}{d\xi} - n^2 X_n = 0 \quad ; \quad X_n(0) = 1 \quad X_n(-\infty) = 0$$

The potential derivatives at the cascade inlet are

$$\frac{\partial \phi}{\partial t} = \Sigma \dot{A}_n e^{in\theta}$$

$$\frac{\partial \phi}{r \partial \theta} = \Sigma A_n \frac{in}{r_1} e^{in\theta}$$

$$\frac{\partial \phi}{\partial m} = \Sigma A_n \frac{n}{r_1}\left(\frac{1}{n}\frac{dX_n}{d\xi}\right)_{m=0} e^{in\theta} = \Sigma A_n \frac{n}{r_1} K_n e^{in\theta}$$

$$\frac{\partial^2 \phi}{\partial m \partial t} = \Sigma \dot{A}_n \frac{n}{r_1} K_n e^{in\theta}$$

With the position

$$J = \frac{b_1 s}{r_1}\int_0^L \frac{dl}{A}$$

we find

$$\dot{A}_n (1 + nK_n J) + \frac{nK_n}{r_1}\left\{(1 - C_p) W_{m_1} - \frac{\partial C_p}{\partial tg\beta_1} tg\beta_1 \frac{W_1^2}{2W_{m_1}}\right\} A_n +$$

$$i\frac{n}{r_1}\left\{(1 - C_p) W_{\theta_1} + \frac{\partial C_p}{\partial tg\beta_1} tg\beta_1 \frac{W_1^2}{2W_{\theta_1}}\right\} A_n = 0$$

Neutral stability conditions are predicted when

$$\frac{\partial C_p}{\partial tg\beta_1} = (1 - C_p) \sin 2\beta_1$$

The stall propagation speed is given by

$$\frac{V_p}{W_{\theta 1}} = \frac{1}{1 + n\kappa_n J} \frac{1 - C_p}{\cos^2 \beta_1}$$

and the corresponding nondimensional frequencies by

$$\frac{\omega_s r_1}{W_{\theta 1}} = \frac{n}{1 + n\kappa_n J} \frac{1 - C_p}{\cos^2 \beta_1}$$

The formulas are strictly valid at the instability onset, but it can be hoped that they maintain their validity even in the initial phase of the phenomenon. The κ_n values are dependent on the width distribution in front of the cascade and deriving general results is not so easy. However, if it is assumed that the width varies monotonically from some value b_1 at $\xi = 0$ to some value b_∞ at $\xi = -\infty$ it can be shown that

$$\frac{db}{d\xi} \gtrless 0$$

results

$$\kappa_n \lessgtr 1$$

So, when the width increases toward the cascade leading edge, a slight frequency increase should be expected. It is however doubtful that this approach could model the crossover geometry: as matter of fact, the experimental results show the opposite trend. For comparison with experimental results, $\kappa_n = 1$ was utilized for any configuration.

As a final remark the following can be noted:
in the case of rotating cascade, assuming zero inlet whirl, the observed non-dimensional frequency is given by

$$\frac{\omega_s}{\Omega} = n - \frac{n}{1 + n\kappa_n J} \frac{1 - C_p}{\cos^2 \beta_1}$$

In the case of stationary cascade, we have directly

$$\frac{\omega_s r_1}{c_{\theta 1}} = \frac{n}{1 + n\kappa_n J} \frac{1 - C_p}{\cos^2 \beta_1}$$

This means that impeller rotating stall must generate frequencies much higher than return channel rotating stall (order of magnitude 0.8 instead of 0.2). In addition, the frequency is expected to decrease when decreasing the flow. Such predictions are confirmed by the experimental results of Ref. 20.

TABLE I

Measuring sect.	Total pressure probes	Static pressure probes	Thermoelements
Sec. 10 (impeller inlet)	4 Kiel 1 Cobra	1	8 (circum. and radially spaced)
Sec. 20 (diffuser inlet)	1 Cobra	1	2 (circum. spaced)
Sec. 40 (diffuser exit)	1 Cobra	4	
Sec. 60 (return channel exit)	4 Kiel	8 (4+4 at inner and over radius)	8 (circum. and radially spaced)

TABLE II

Measuring sect.	Total pressure probes	Static pressure probes
Sec. 10' (impeller inlet)	1	1
Sec. 20' (diffuser inlet)	1	2 (90° spaced)
Sec. 30' (diffuser midspan)	1	2 (90° spaced)
Sec. 40' (diffuser exit)		2 (90° spaced)
Sec. 50' (return channel throat area)		2 (90° spaced. Throat area of two sections of the return channel)
Sec. 60' (return channel exit)		1 (at the exit of one of the two sections of sec. 50')

TABLE III

Impeller Outlet Width	:	0.050			
Diffuser Inlet Width	:	0.0311			
Diffuser Exit Width	:	0.0256			
			Configurations		
		A	B	C	D
Return Channel Inlet Width	:	0.0278	0.0400	0.0400	0.0278
Return Channel Outlet Width	:	0.0400	0.0522	0.0522	0.0400
Return Channel Inlet Angle	:	18°	18°	14°.5	14°.5

(All dimensions are referred to impeller external diameter)

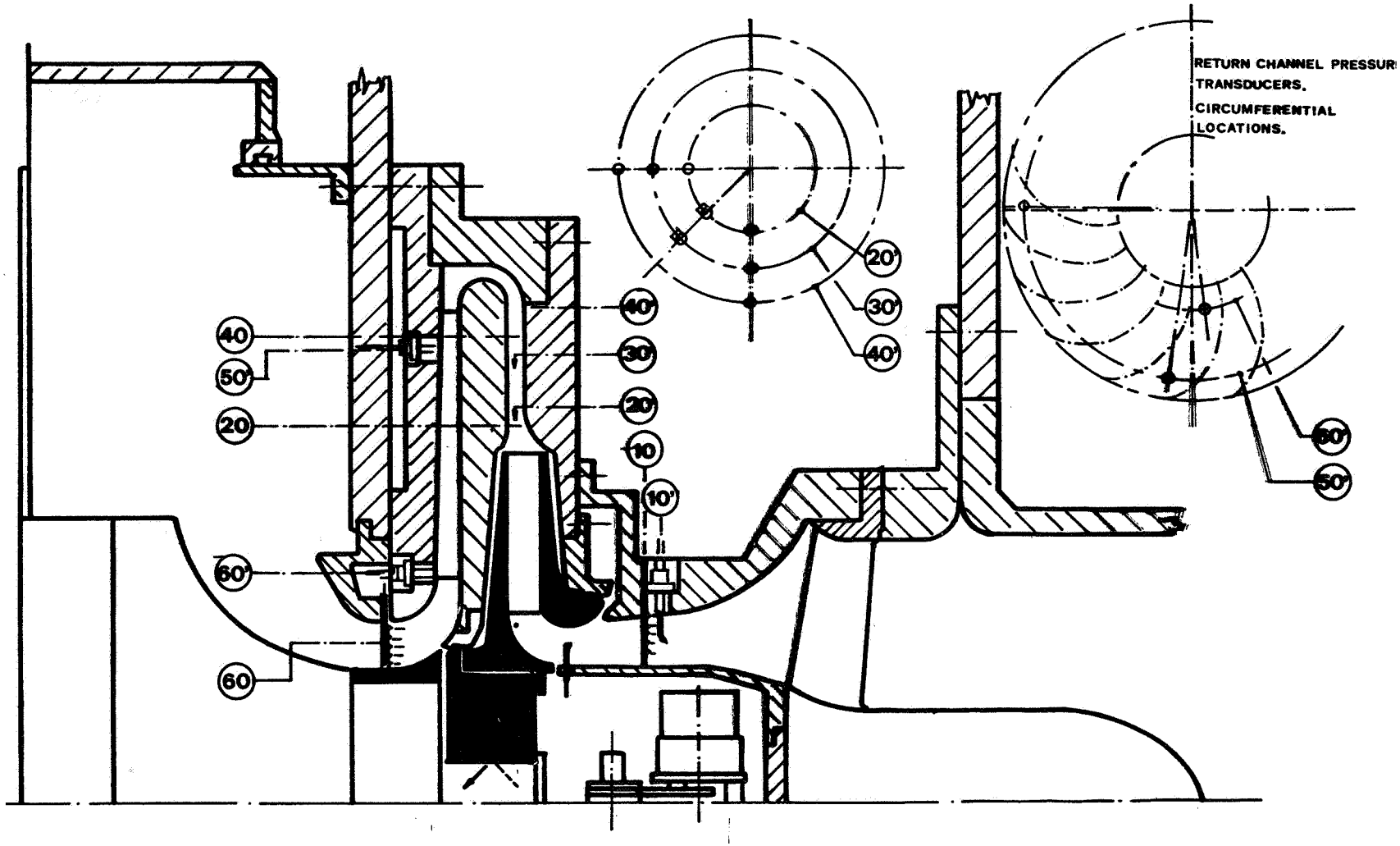

Figure 1. - Cross section of test rig.

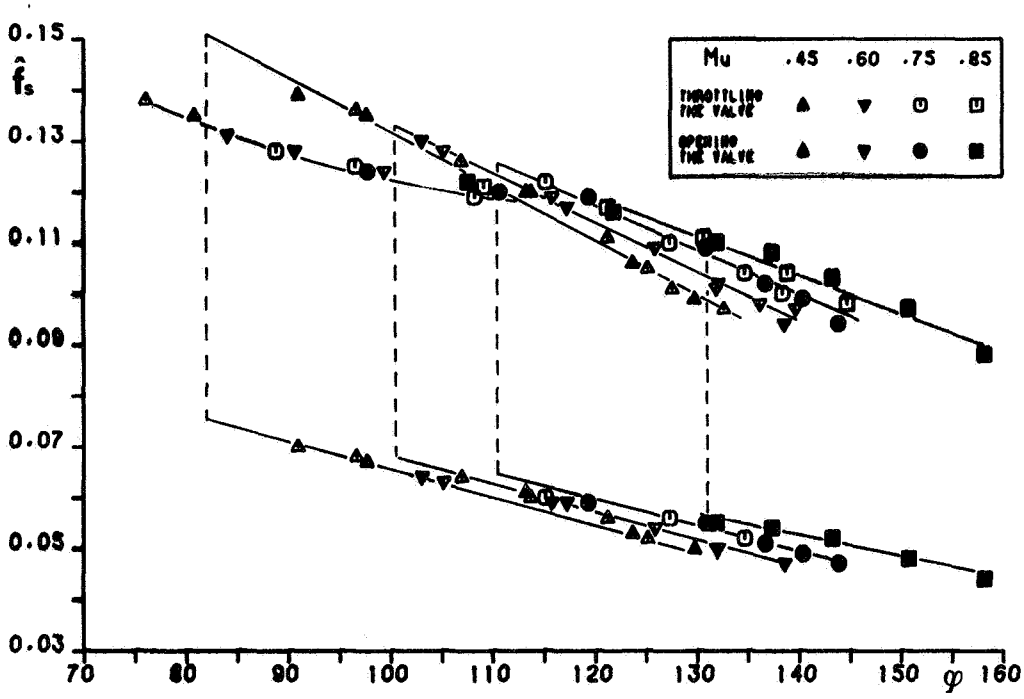

Figure 2. - Normalized observed frequency versus inlet flow coefficient. (Configuration A.)

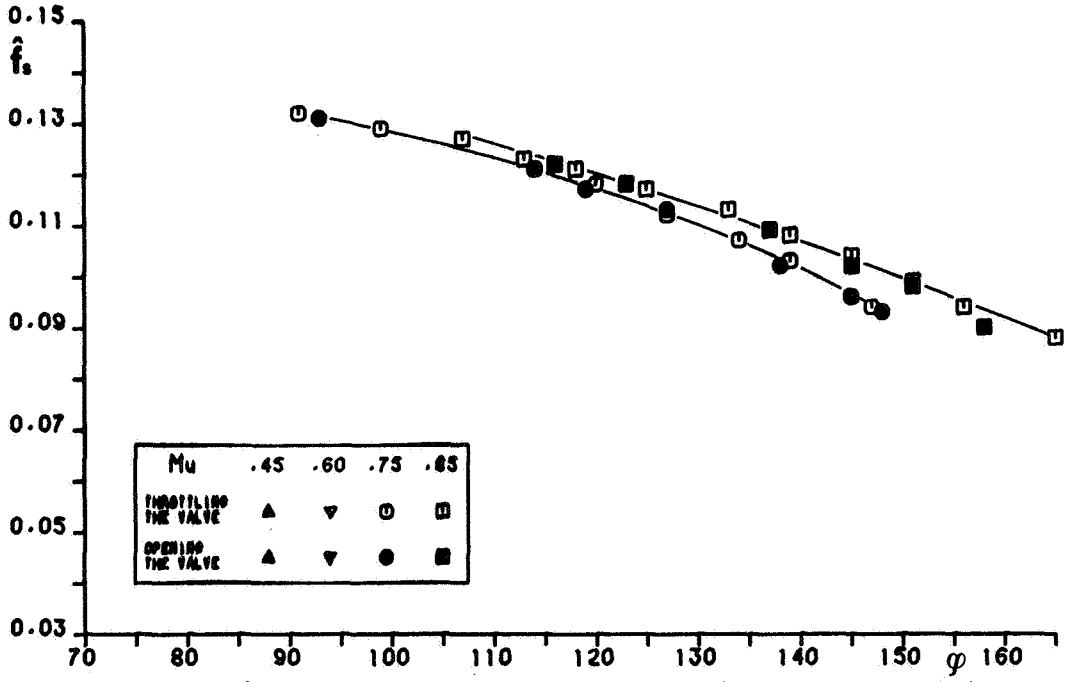

Figure 3. - Normalized observed frequency versus inlet flow coefficient. (Configuration A with sandpaper.)

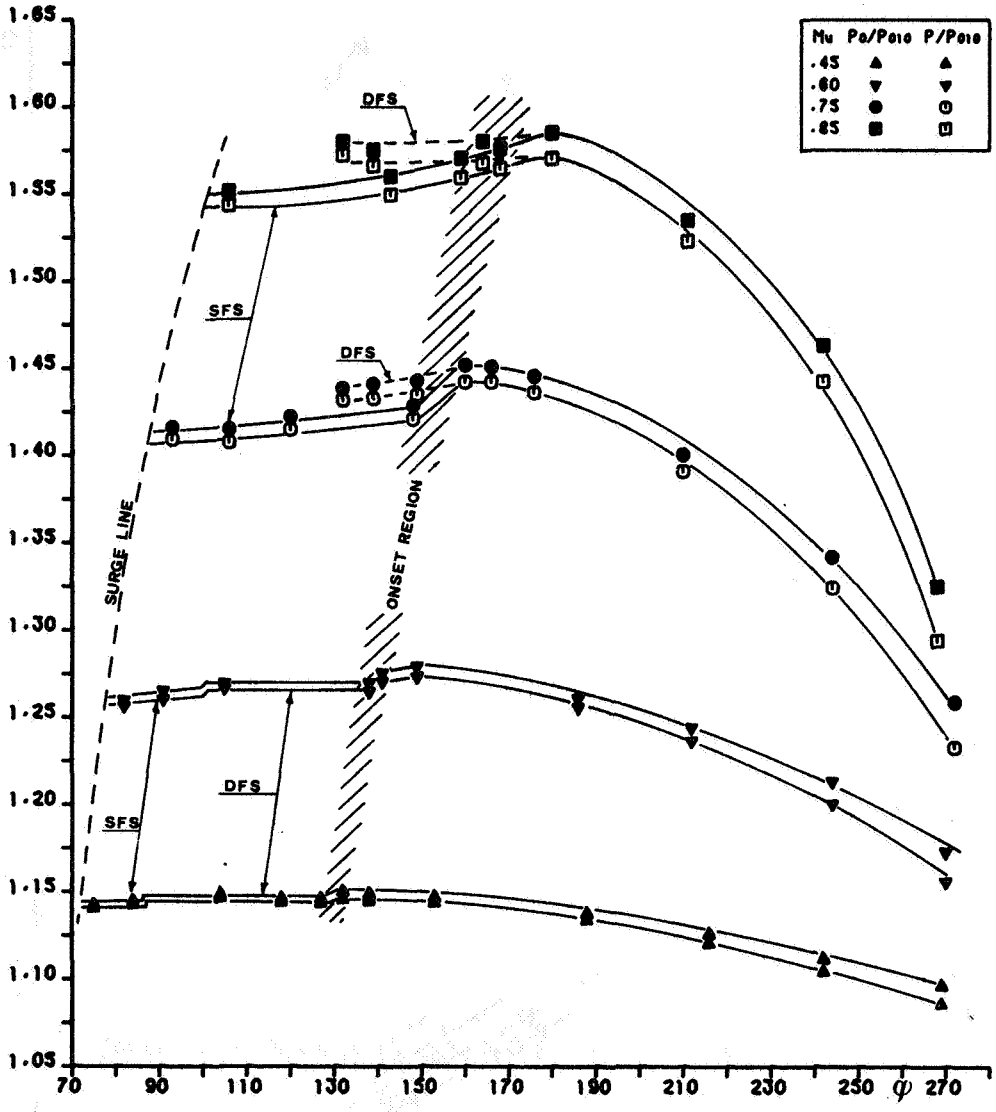

Figure 4. - Static-to-total and total-to-total pressure ratios at section 60 versus inlet flow coefficient. (Configuration A.)

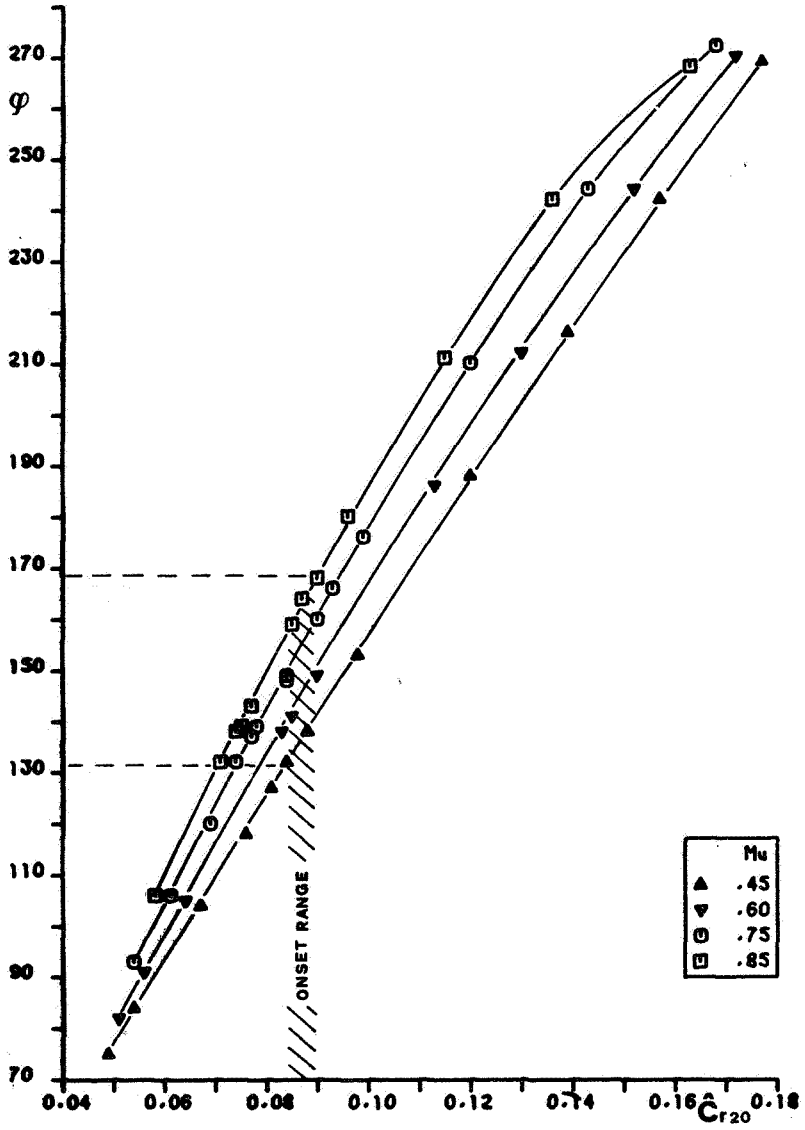

Figure 5. - Inlet flow coefficient versus nondimensional radial velocity at section 20. (Configuration A.)

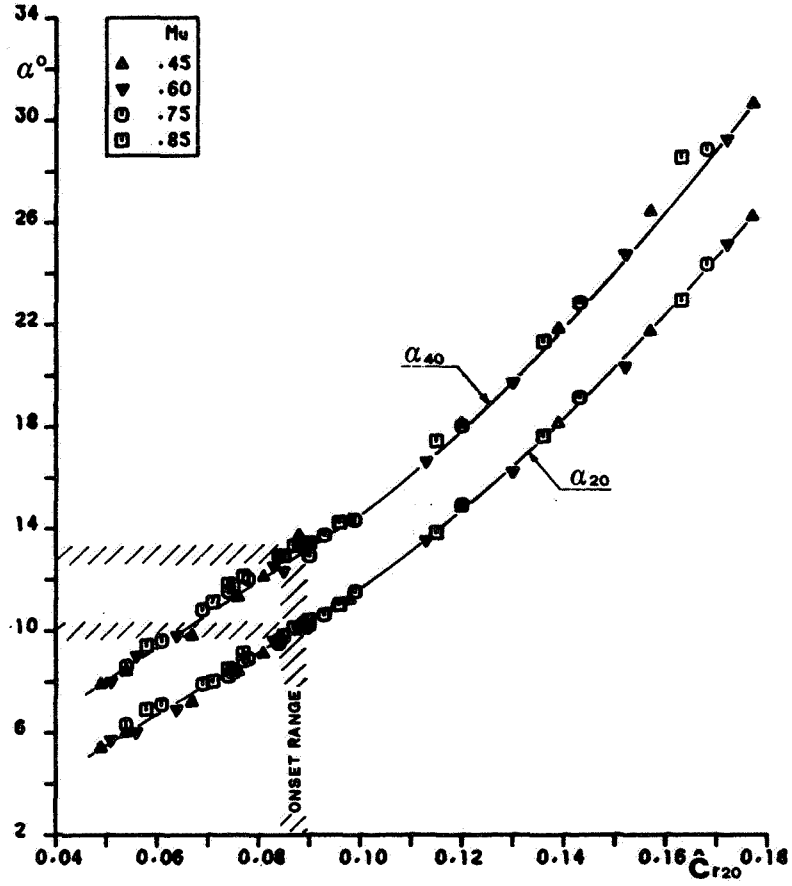

Figure 6. - Absolute flow angles at sections 20 and 40 versus nondimensional radial velocity at section 20. (Configuration A.)

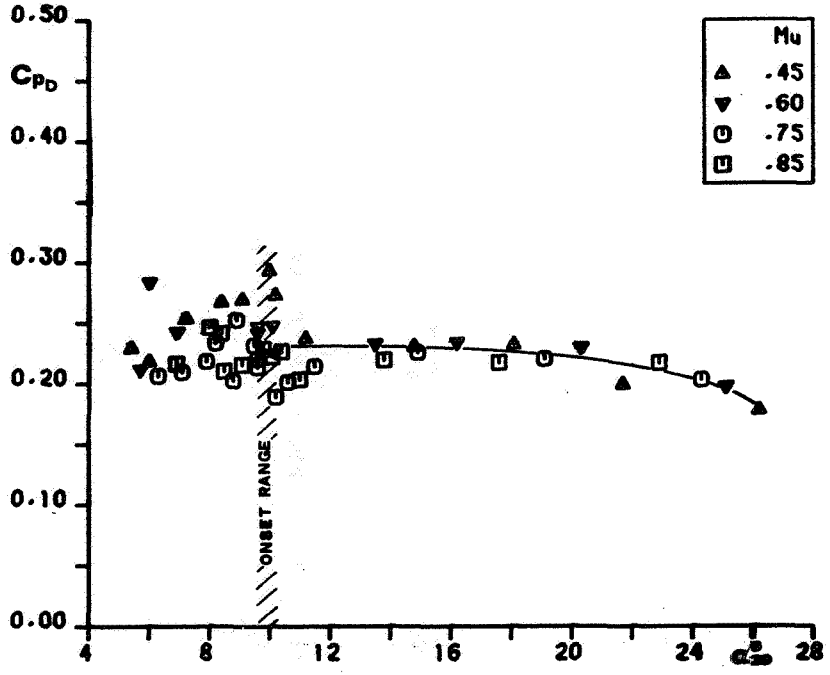

Figure 7. - Vaneless diffuser pressure recovery coefficient versus absolute flow angle at section 20. (Configuration A.)

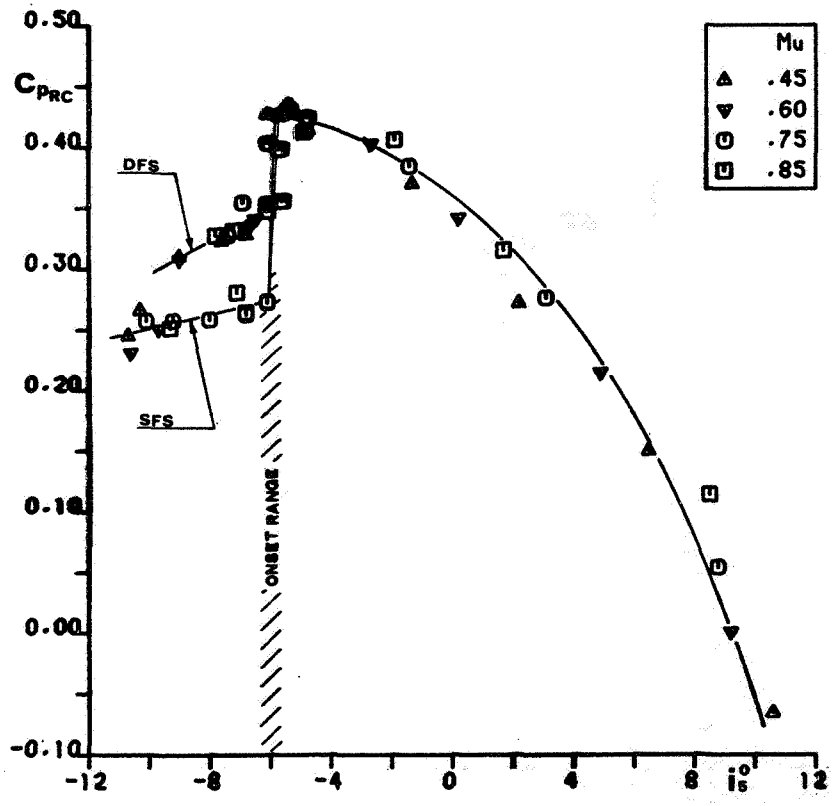

Figure 8. - Return channel pressure recovery coefficient versus incidence angle. (Configuration A.)

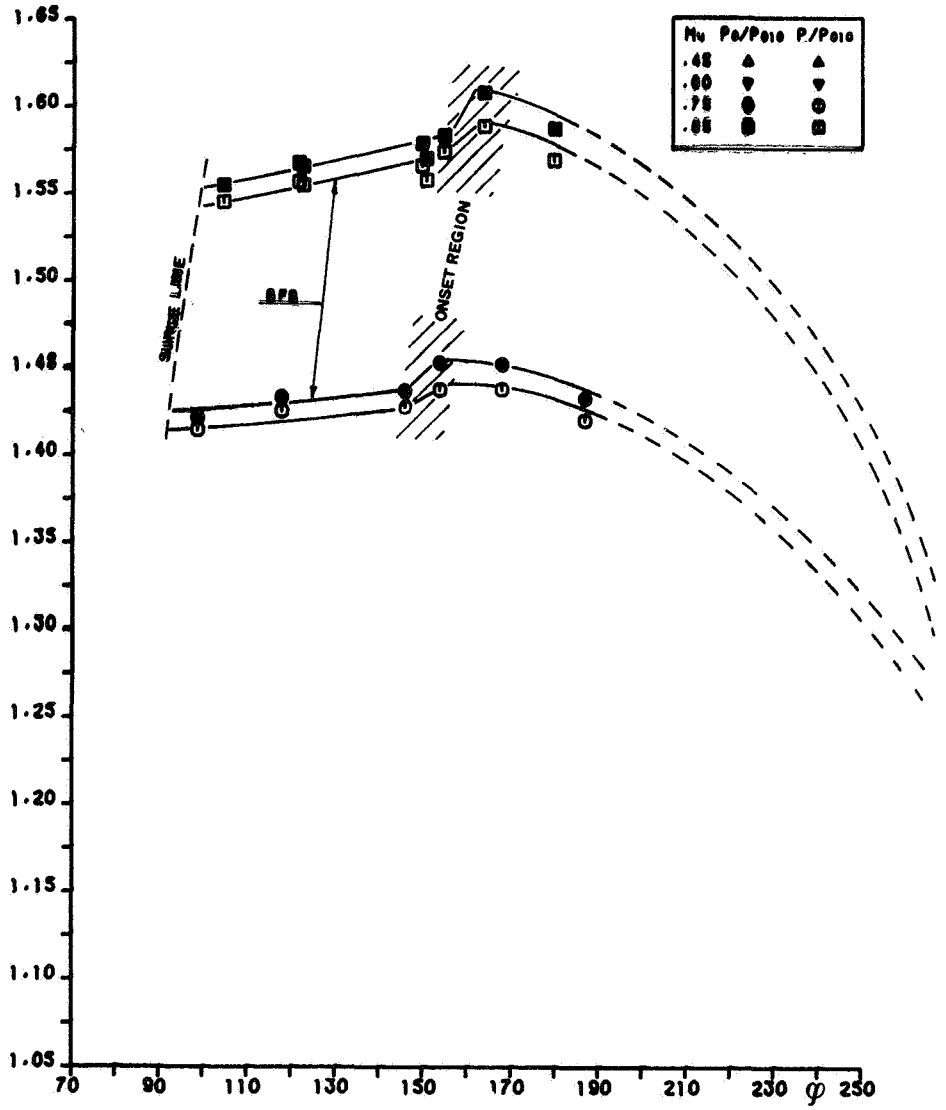

Figure 9. - Static-to-total and total-to-total pressure ratios at section 60 versus inlet flow coefficient. (Configuration A with sandpaper.)

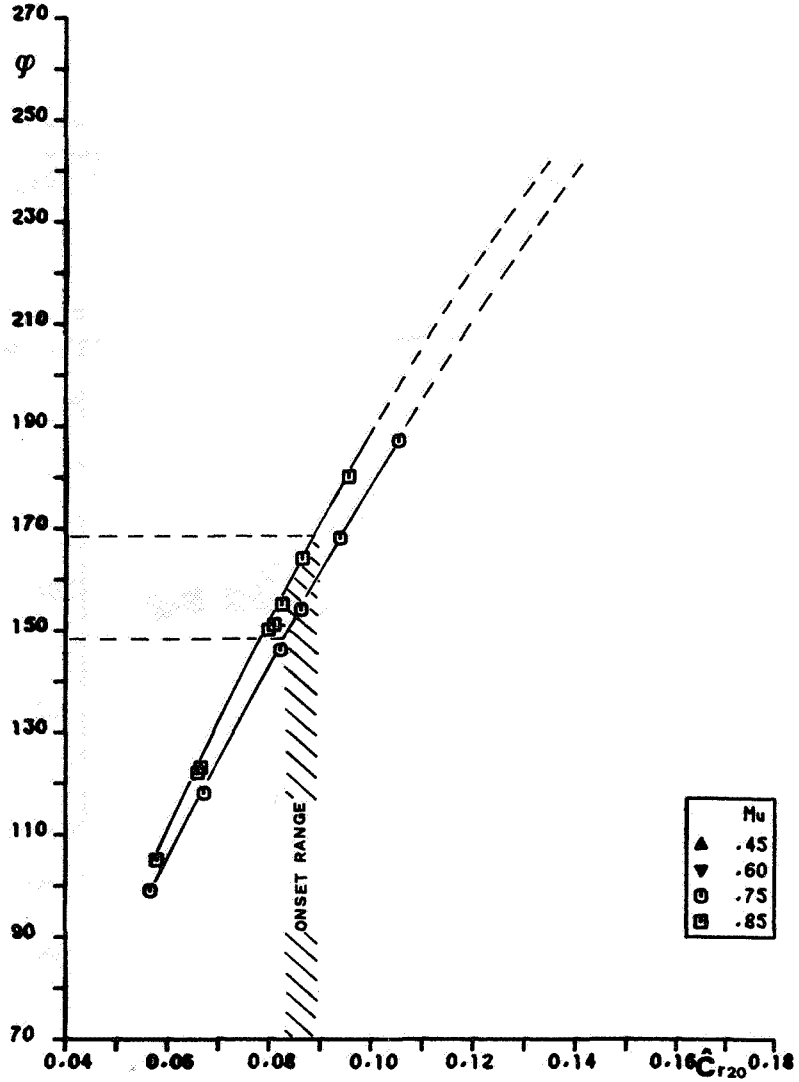

Figure 10. - Inlet flow coefficient versus nondimensional radial velocity at section 20. (Configuration A with sandpaper.)

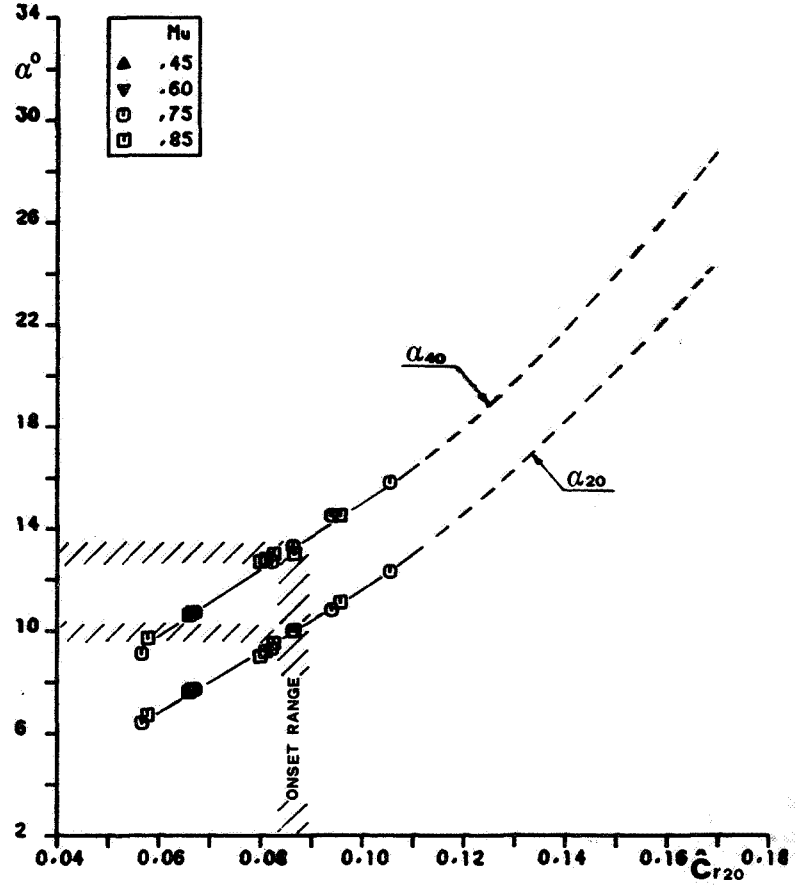

Figure 11. - Absolute flow angles at sections 20 and 40 versus nondimensional radial velocity at section 20. (Configuration A with sandpaper.)

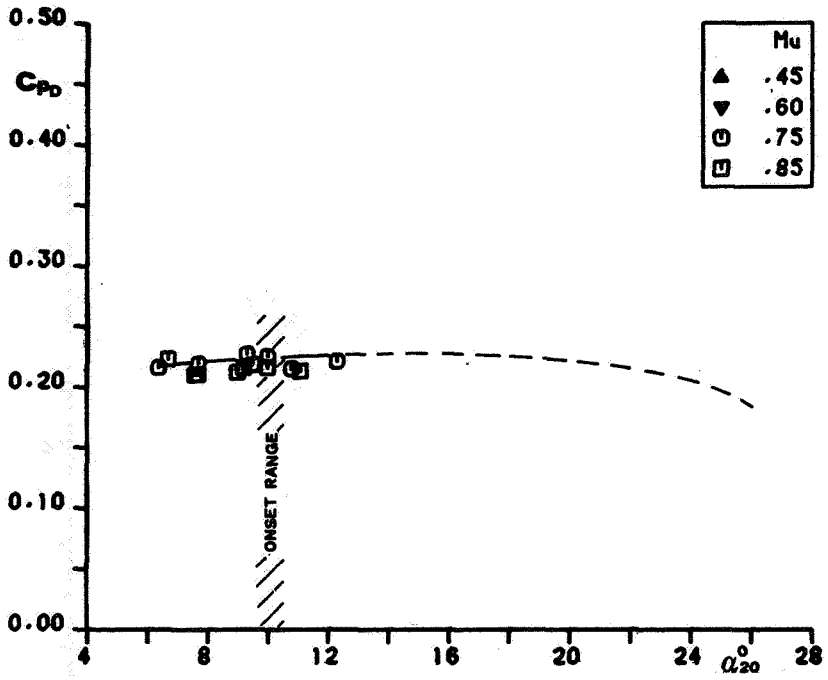

Figure 12. - Vaneless diffuser pressure recovery coefficient versus absolute flow angle at section 20. (Configuration A with sandpaper.)

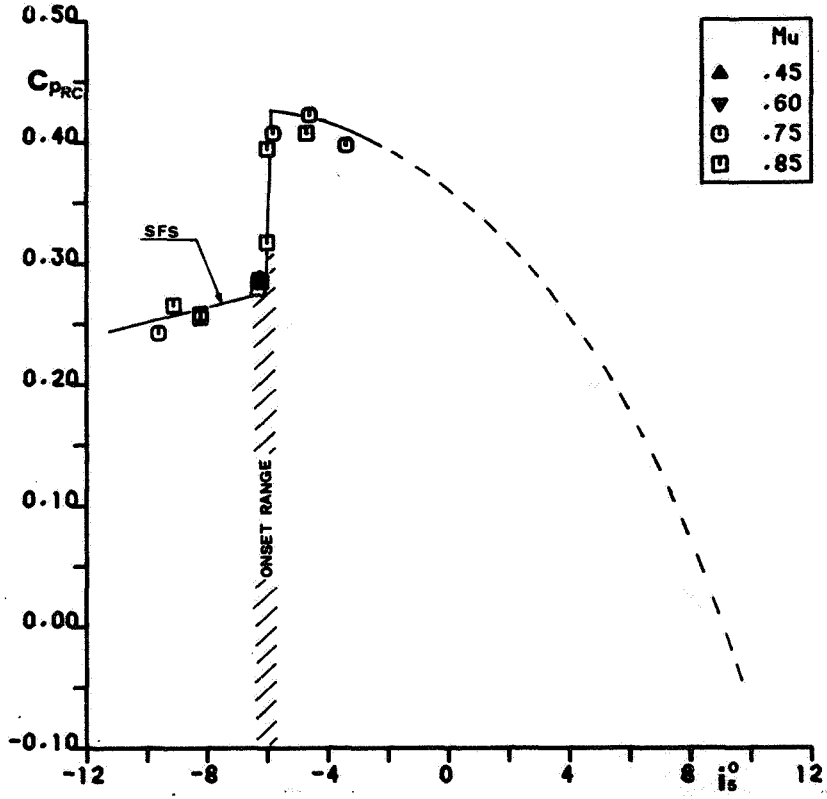

Figure 13. - Return channel pressure recovery coefficient versus incidence angle. (Configuration A with sandpaper.)

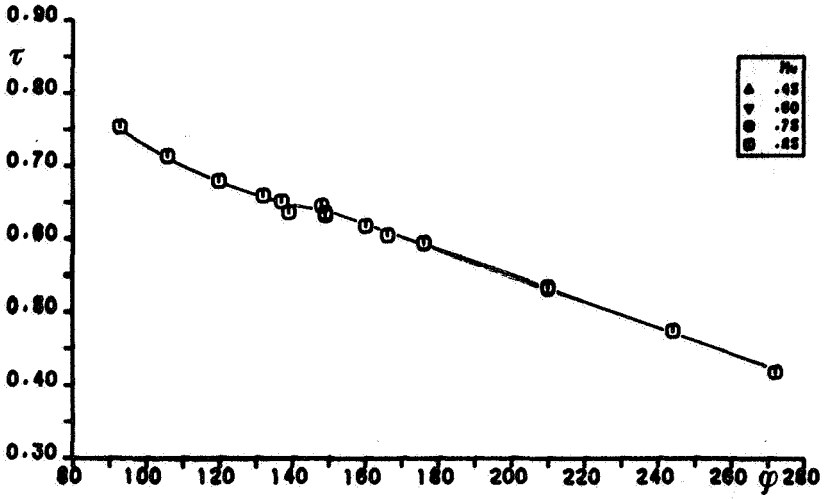

Figure 14. - Total enthalpy rise coefficient versus inlet flow coefficient. (Configuration A.)

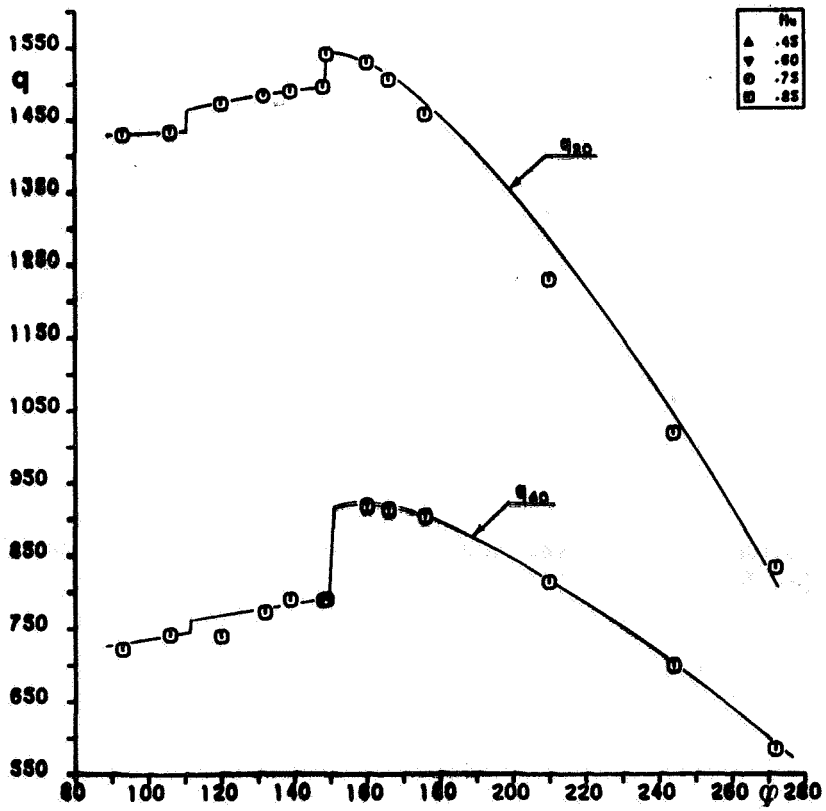

Figure 15. - Dynamic pressure at sections 20 and 40 versus inlet flow coefficient. (Configuration A.)

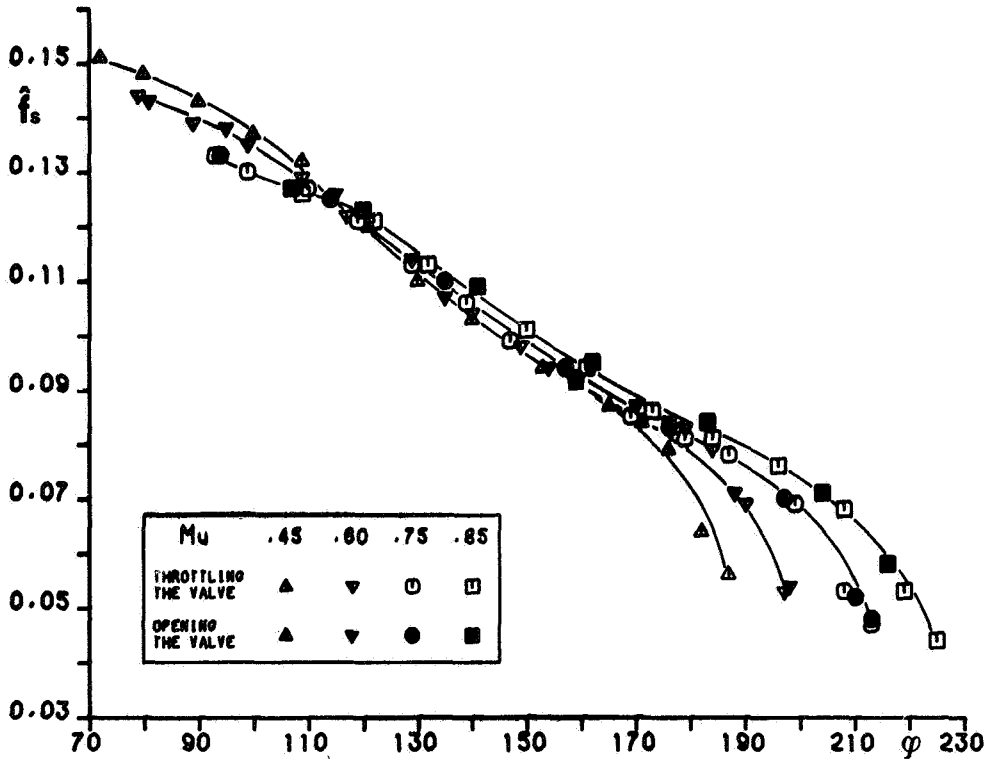

Figure 16. - Normalized observed frequency versus inlet flow coefficient. (Configuration B.)

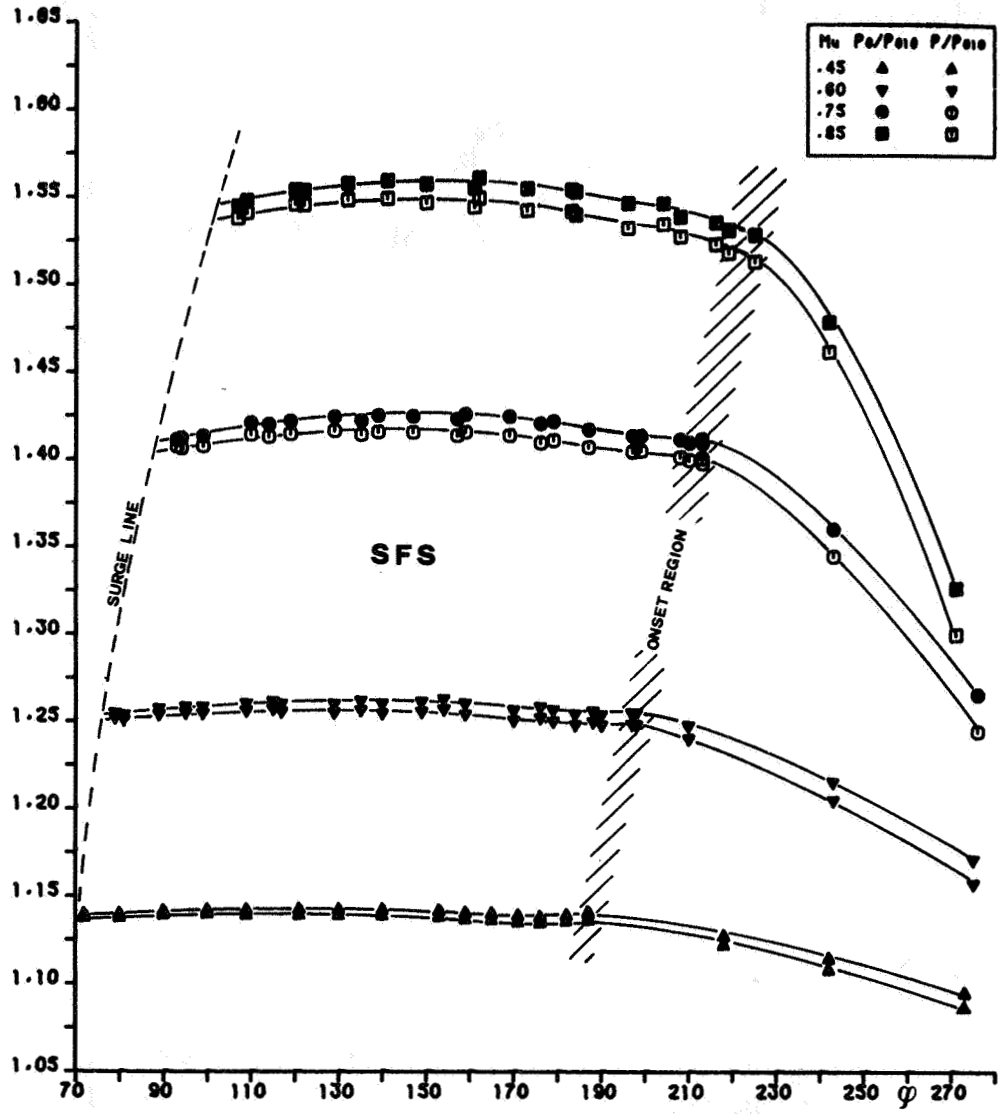

Figure 17. - Static-to-total and total-to-total pressure ratios at section 60 versus inlet flow coefficient. (Configuration B.)

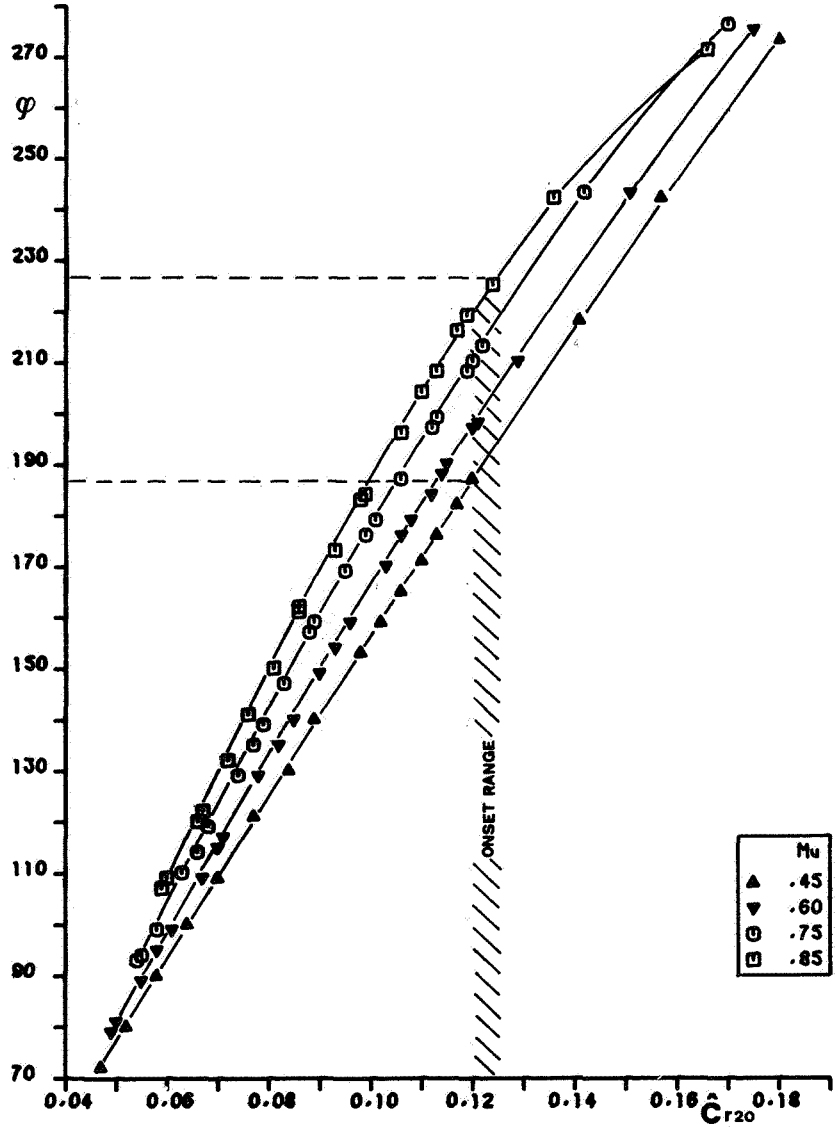

Figure 18. - Inlet flow coefficient versus nondimensional radial velocity at section 20. (Configuration B.)

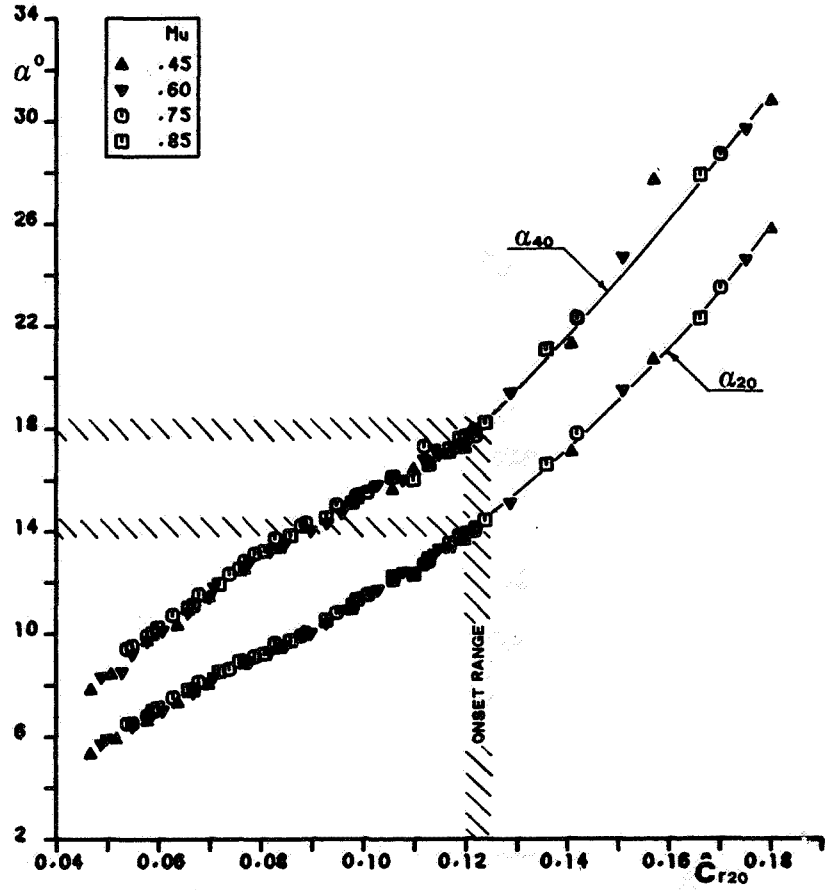

Figure 19. - Absolute flow angles at sections 20 and 40 versus nondimensional radial velocity at section 20. (Configuration B.)

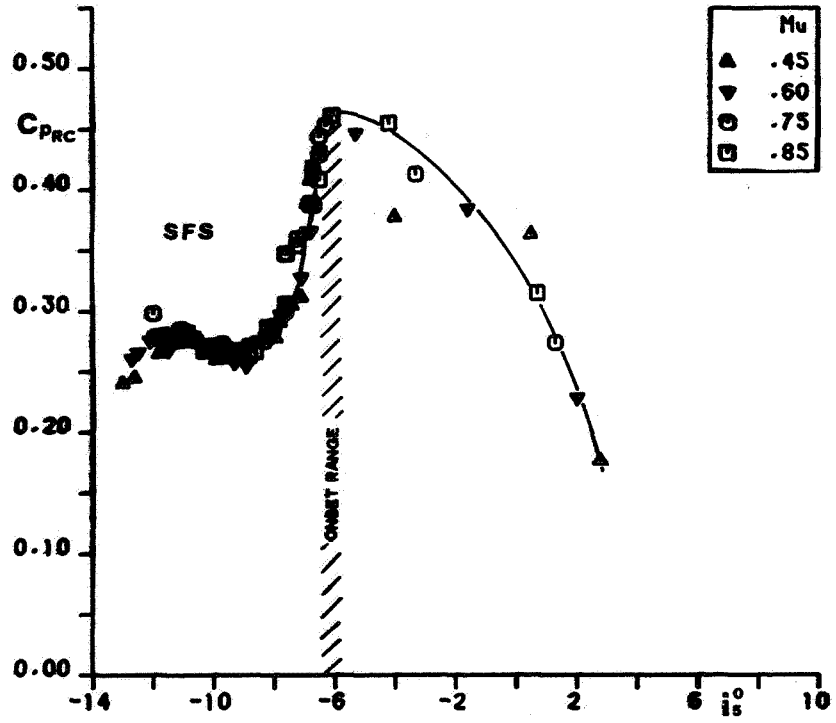

Figure 20. - Return channel pressure recovery coefficient versus incidence angle. (Configuration B.)

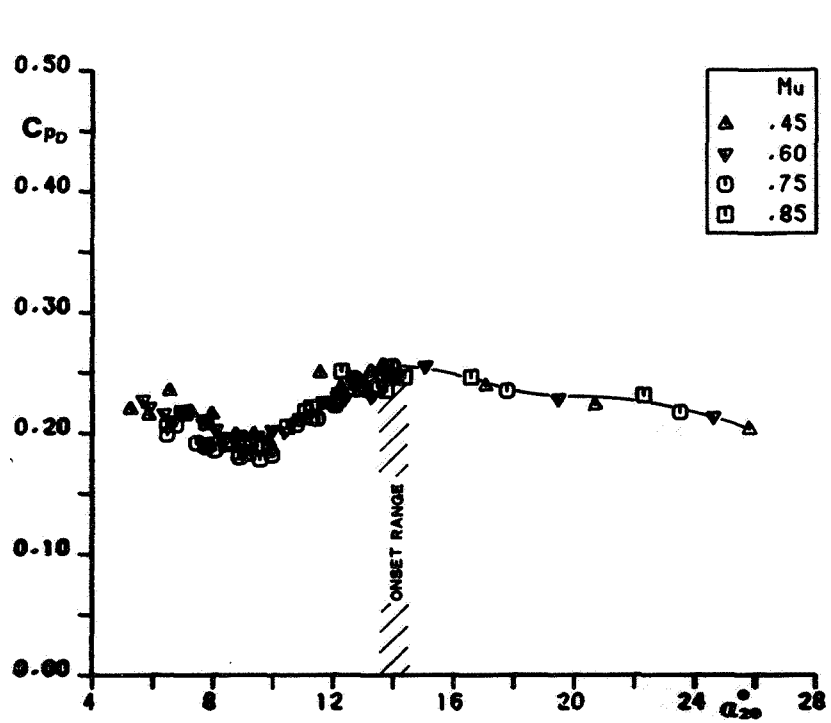

Figure 21. - Vaneless diffuser pressure recovery coefficient versus absolute flow angle at section 20. (Configuration B.)

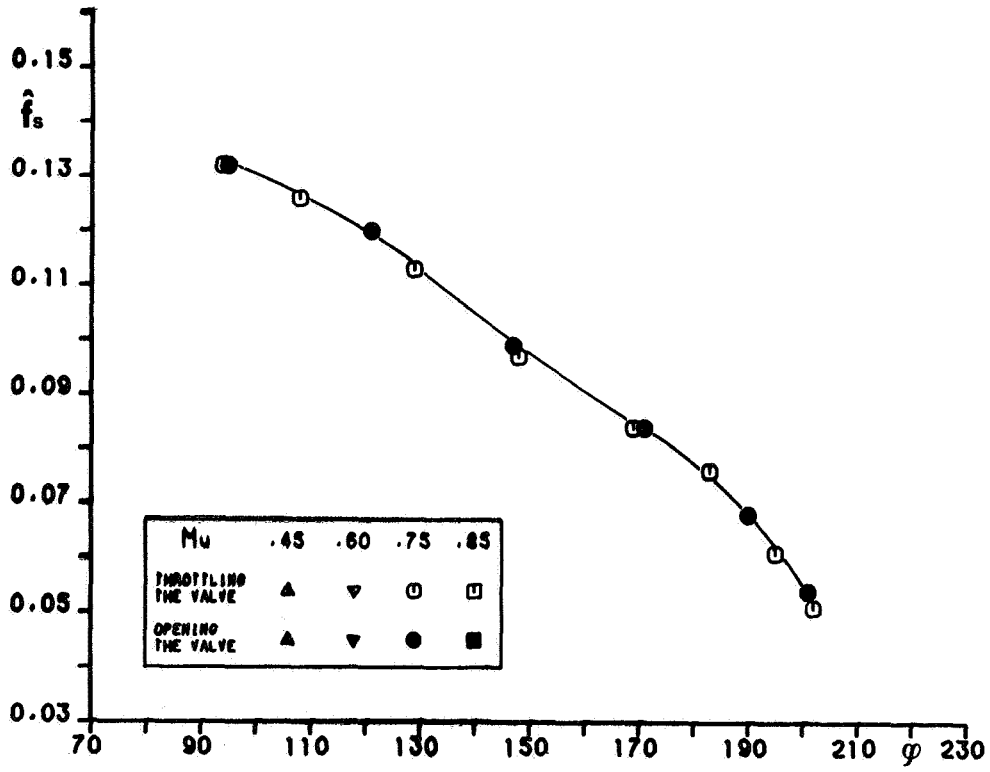

Figure 22. - Normalized observed frequency versus inlet flow coefficient. (Configuration C.)

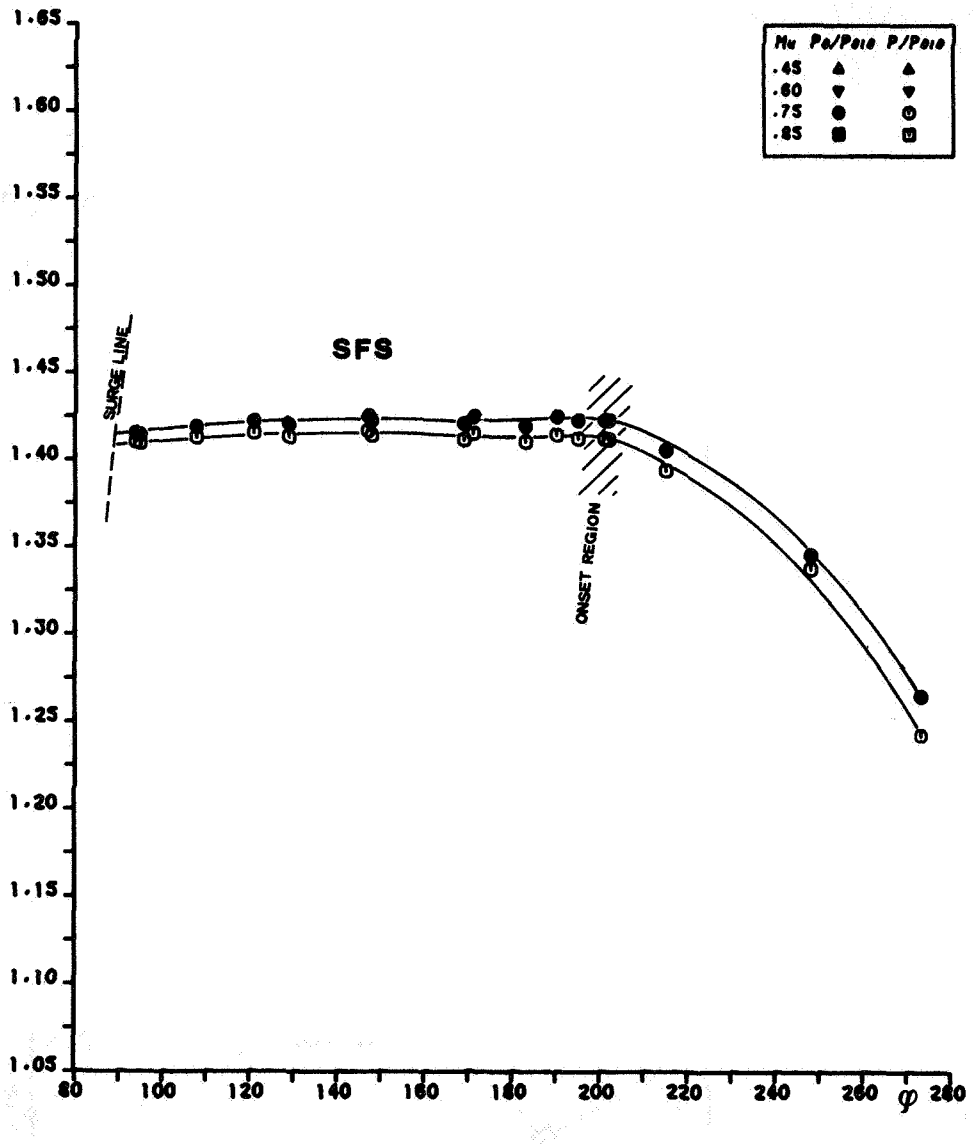

Figure 23. - Static-to-total and total-to-total pressure ratios at section 60 versus inlet flow coefficient. (Configuration C.)

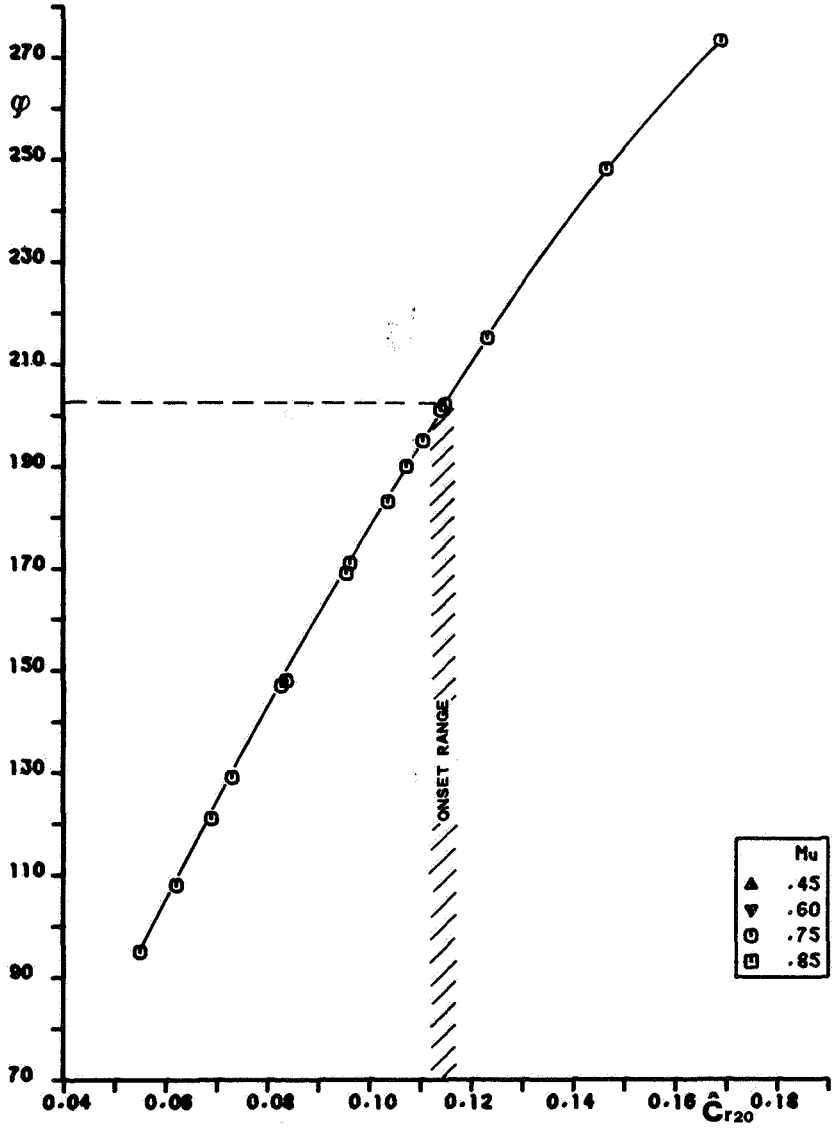

Figure 24. - Inlet flow coefficient versus nondimensional radial velocity at section 20. (Configuration C.)

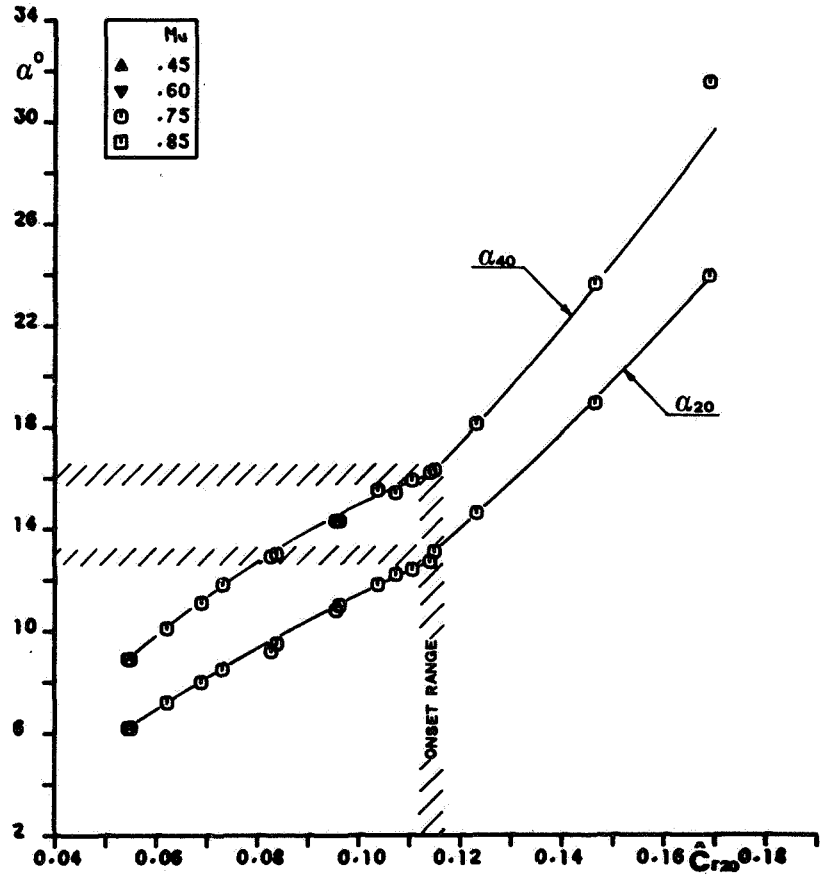

Figure 25. - Absolute flow angles at sections 20 and 40 versus nondimensional radial velocity at section 20. (Configuration C.)

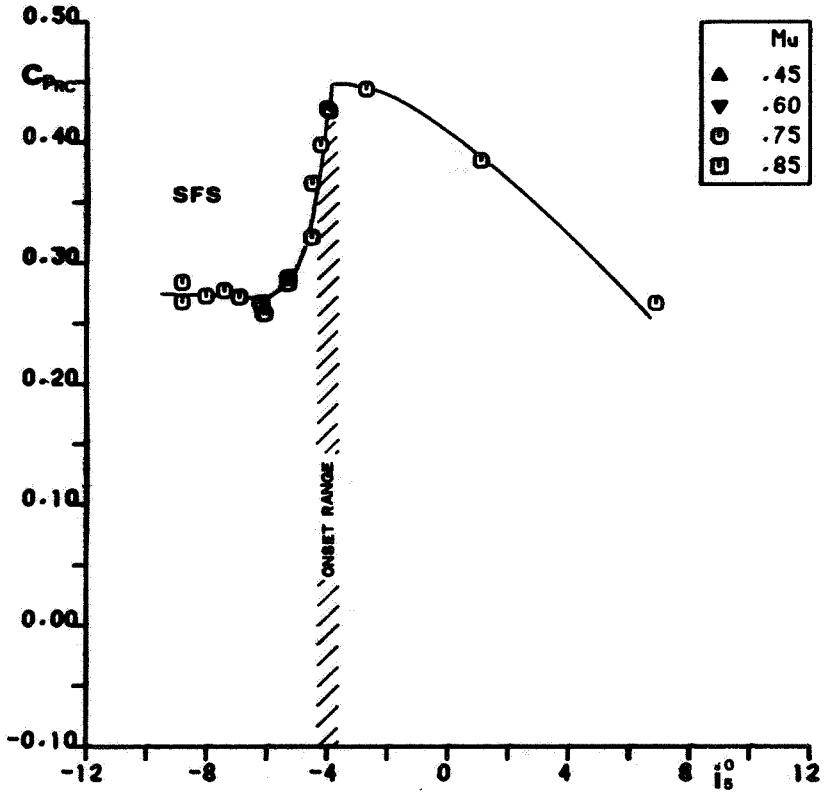

Figure 26. - Return channel pressure recovery coefficient versus incidence angle. (Configuration C.)

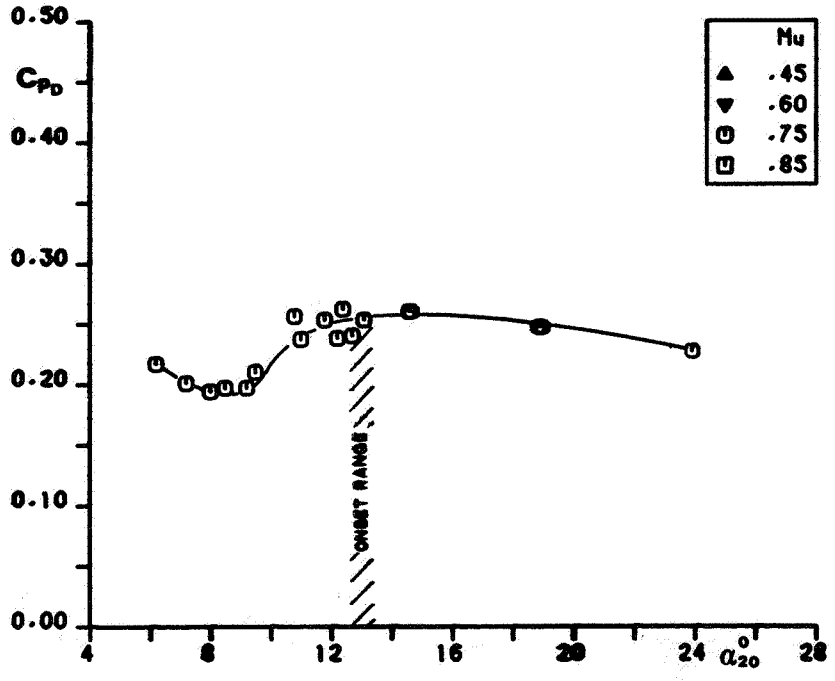

Figure 27. - Vaneless diffuser pressure recovery coefficient versus absolute flow angle at section 20. (Configuration C.)

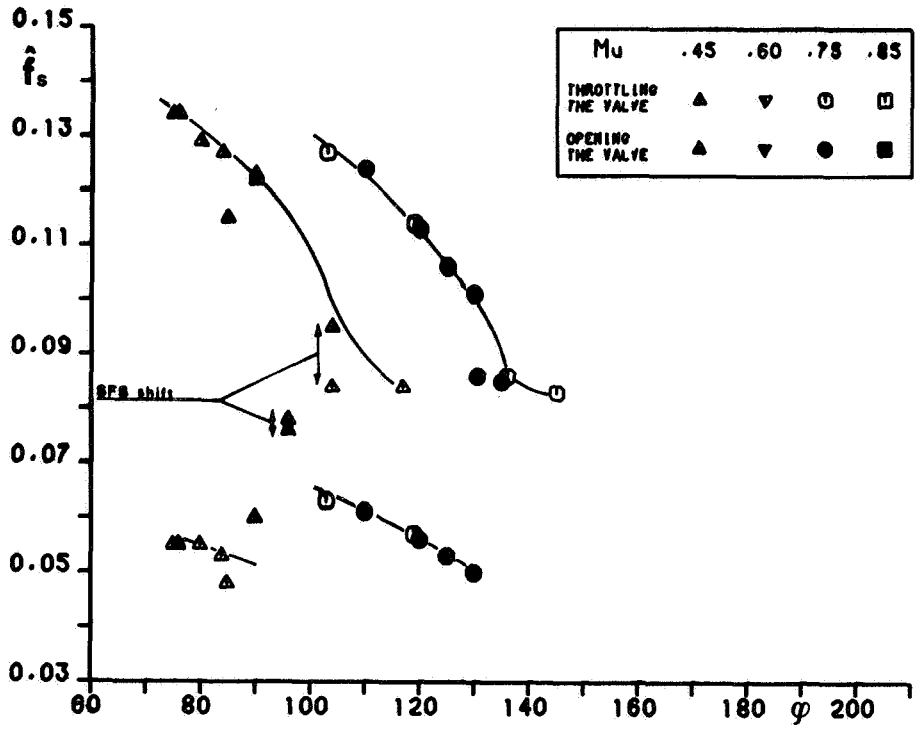

Figure 28. - Normalized observed frequency versus inlet flow coefficient. (Configuration D.)

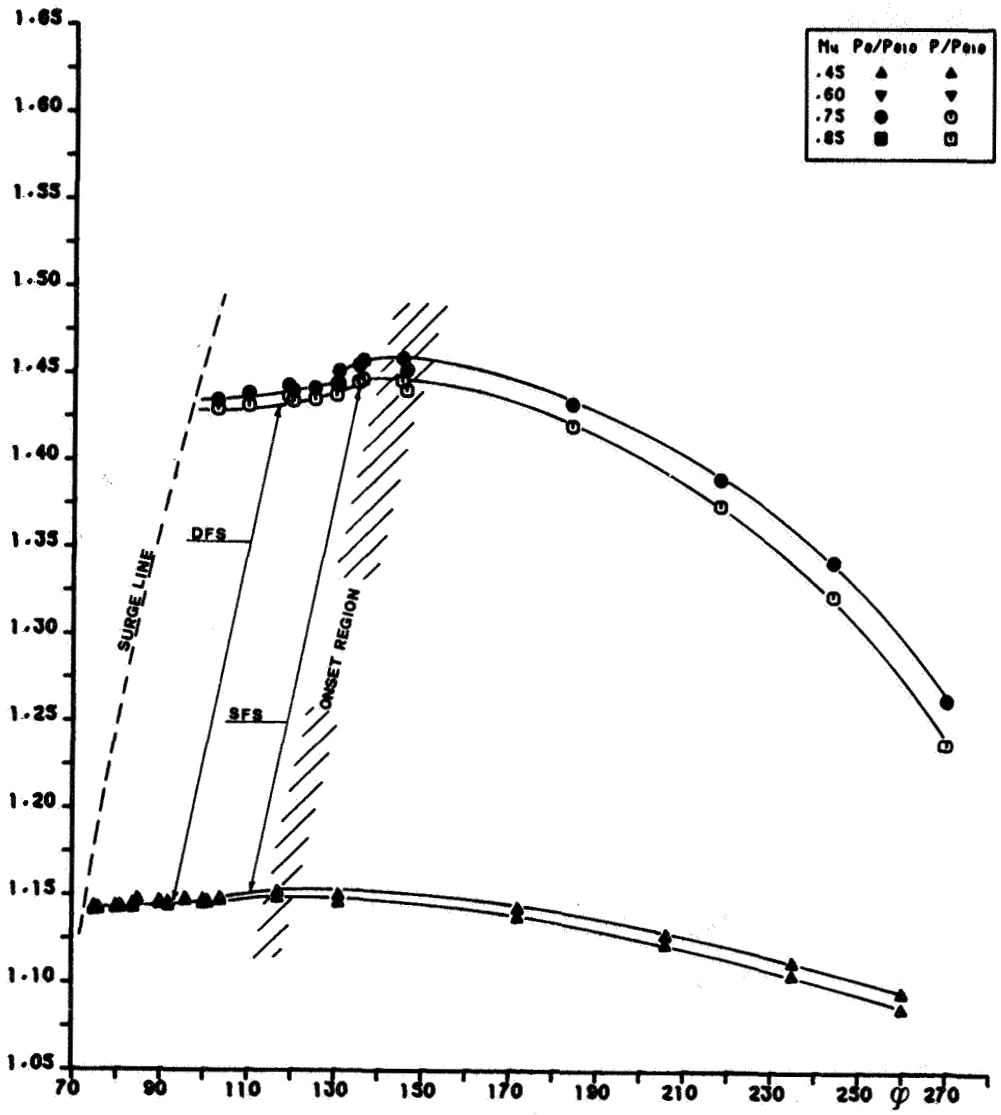

Figure 29. - Static-to-total and total-to-total pressure ratios at section 60 versus inlet flow coefficient. (Configuration D.)

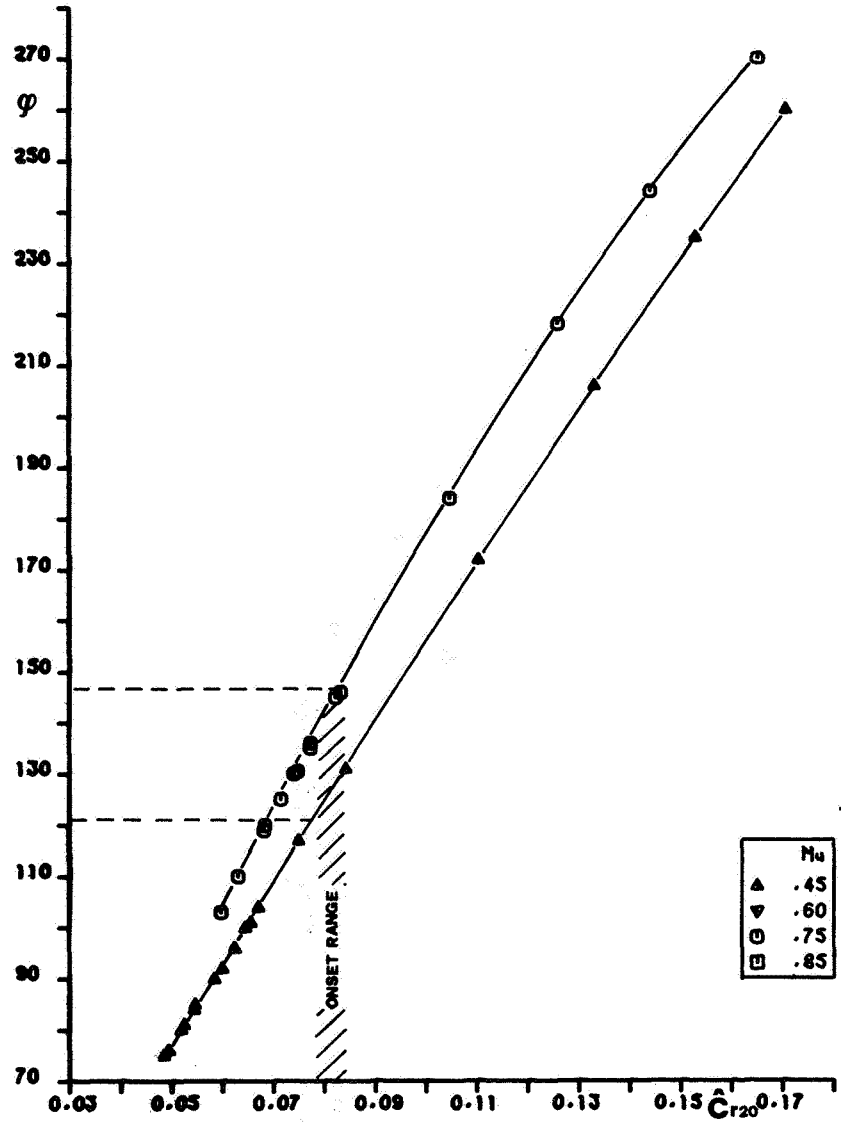

Figure 30. - Inlet flow coefficient versus nondimensional radial velocity at section 20. (Configuration D.)

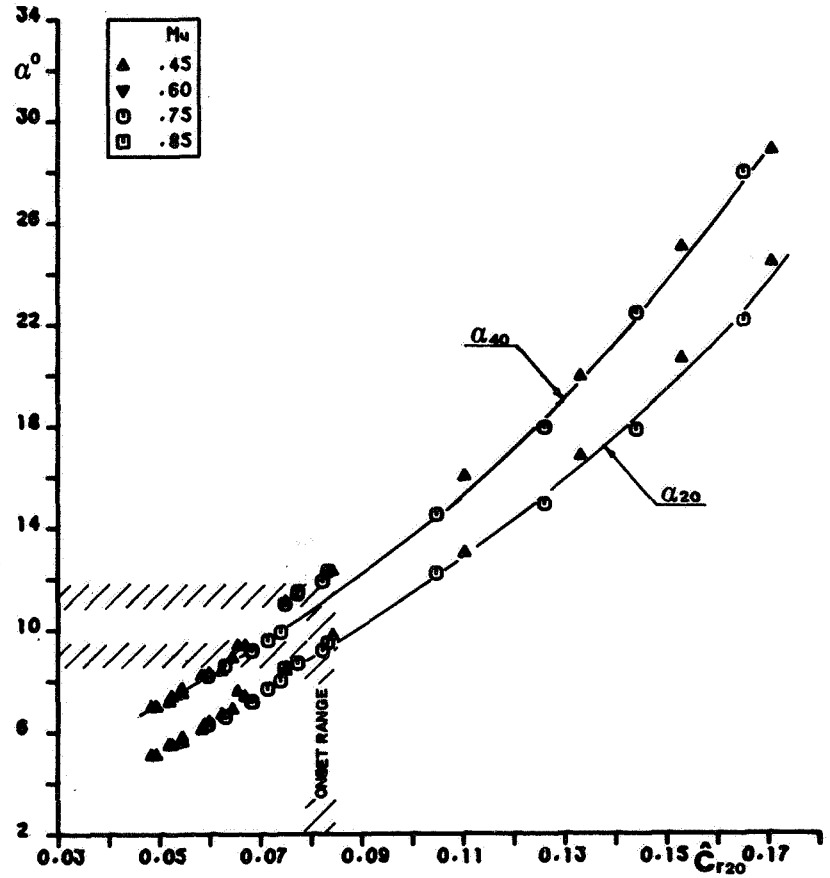

Figure 31. - Absolute flow angles at sections 20 and 40 versus nondimensional radial velocity at section 20. (Configuration D.)

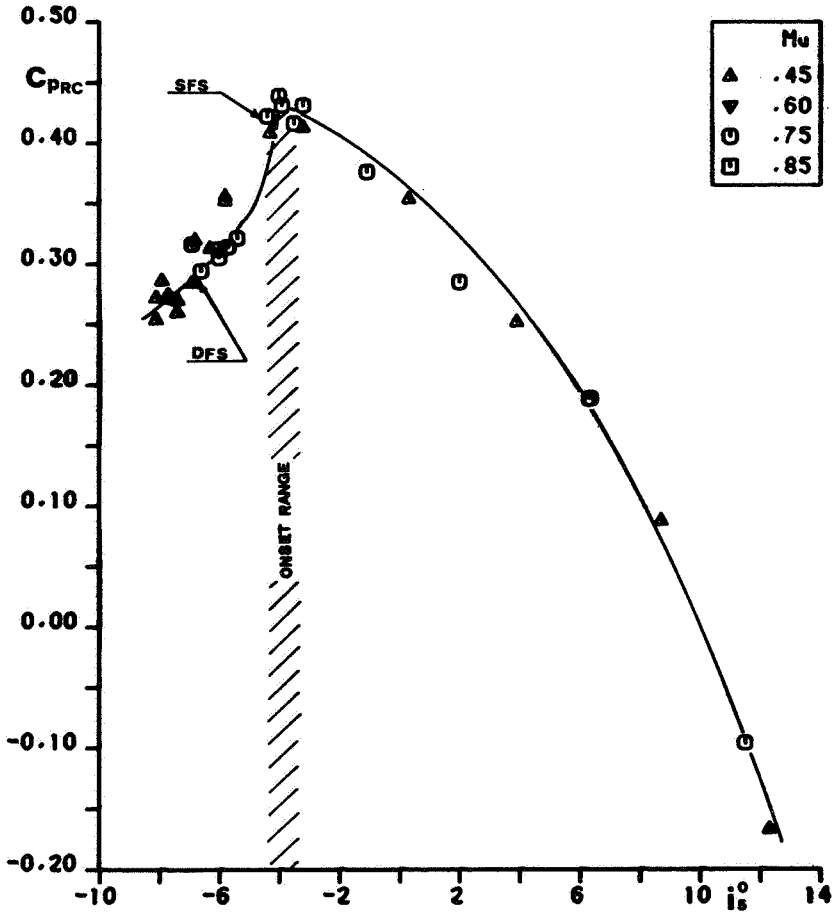

Figure 32. - Return channel pressure recovery coefficient versus incidence angle. (Configuration D.)

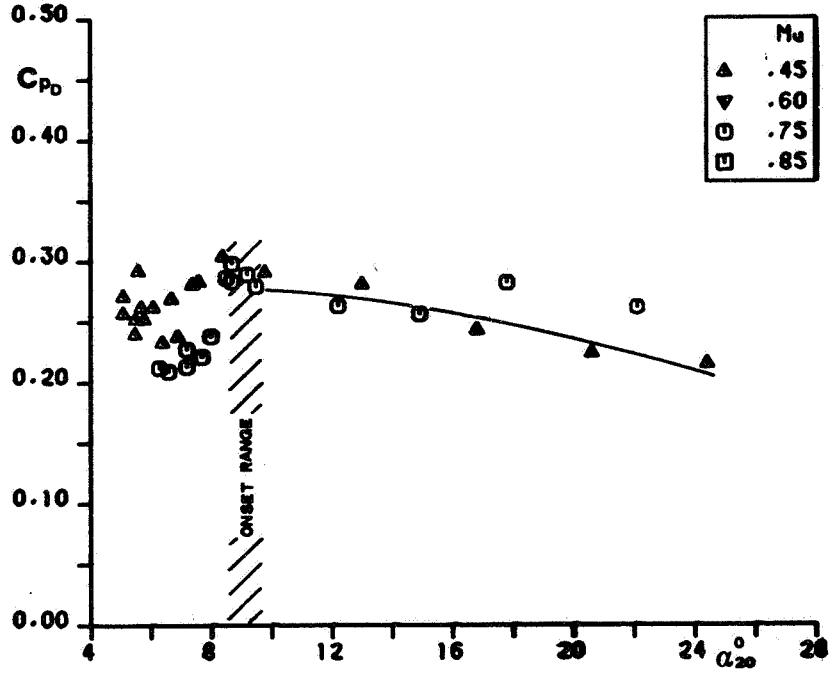

Figure 33. - Vaneless diffuser pressure recovery coefficient versus absolute flow angle at section 20. (Configuration D.)

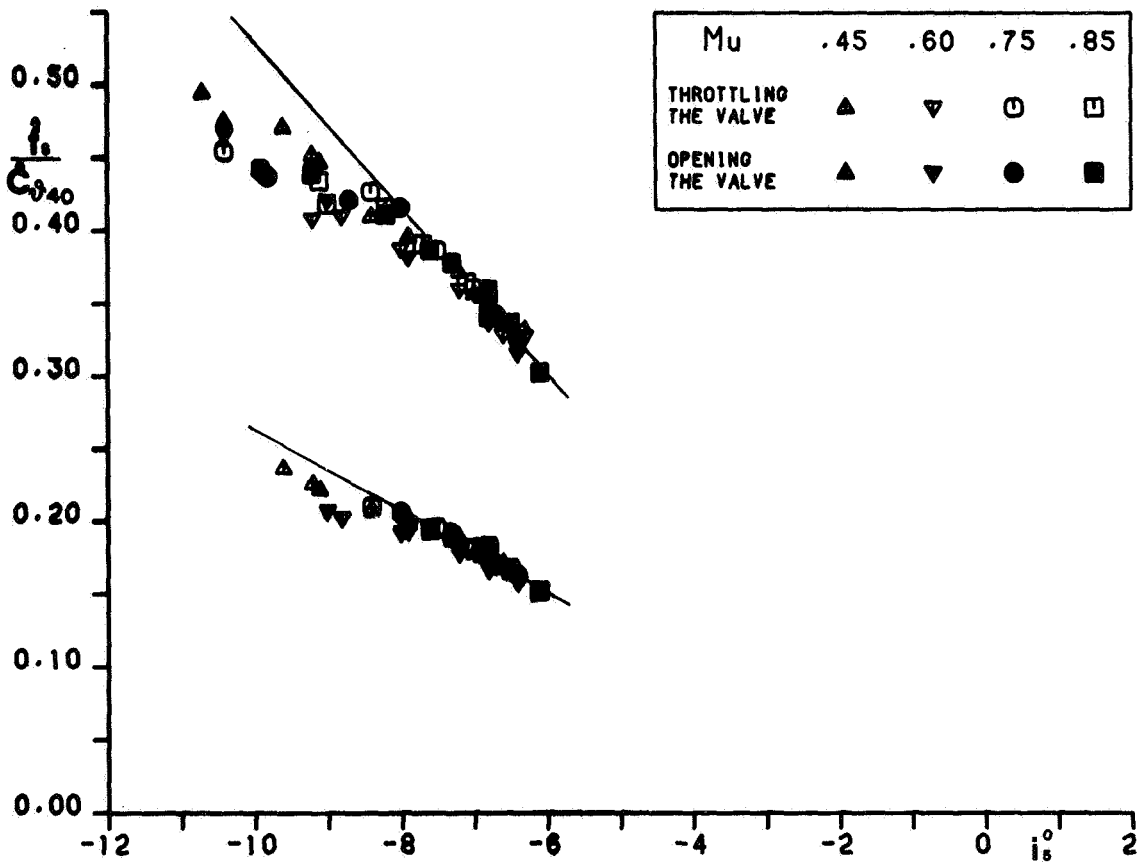

Figure 34. - Nondimensional frequency versus incidence angle. (Configuration A.)

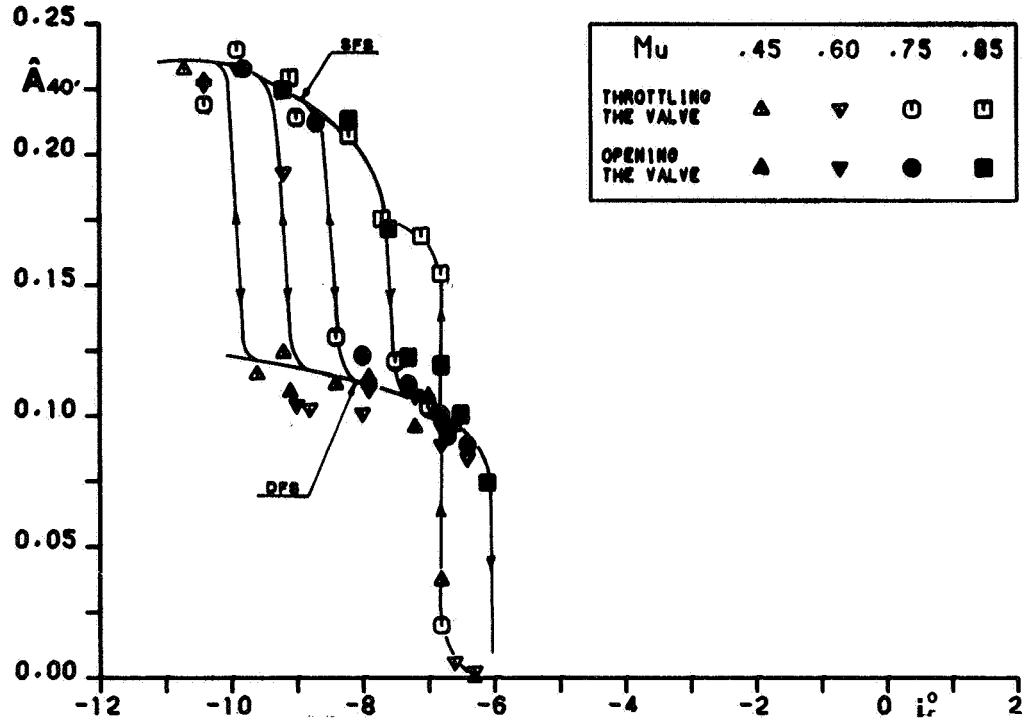

Figure 35. - Nondimensional amplitude (fs) at section 40' versus incidence angle. (Configuration A.)

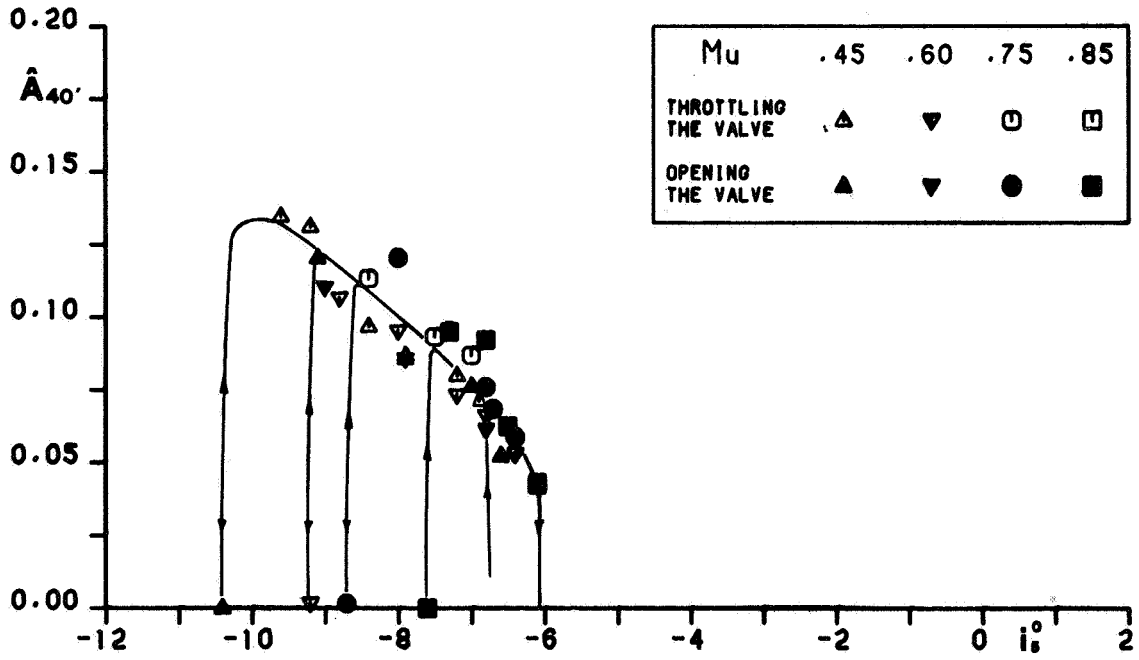

Figure 36. - Nondimensional amplitude (fs/2) at section 40' versus incidence angle. (Configuration A.)

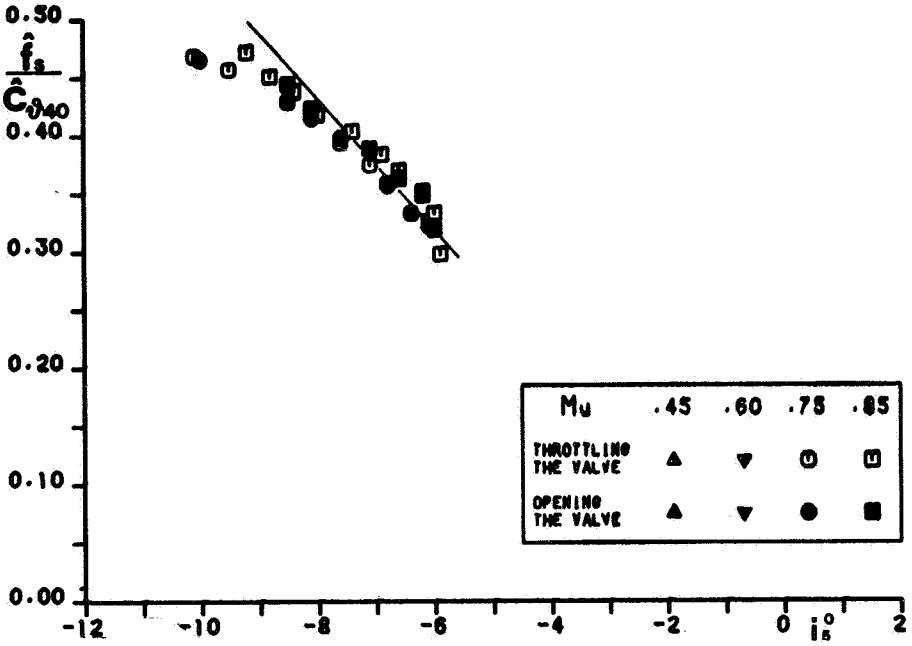

Figure 37. - Nondimensional frequency versus incidence angle. (Configuration A with sandpaper.)

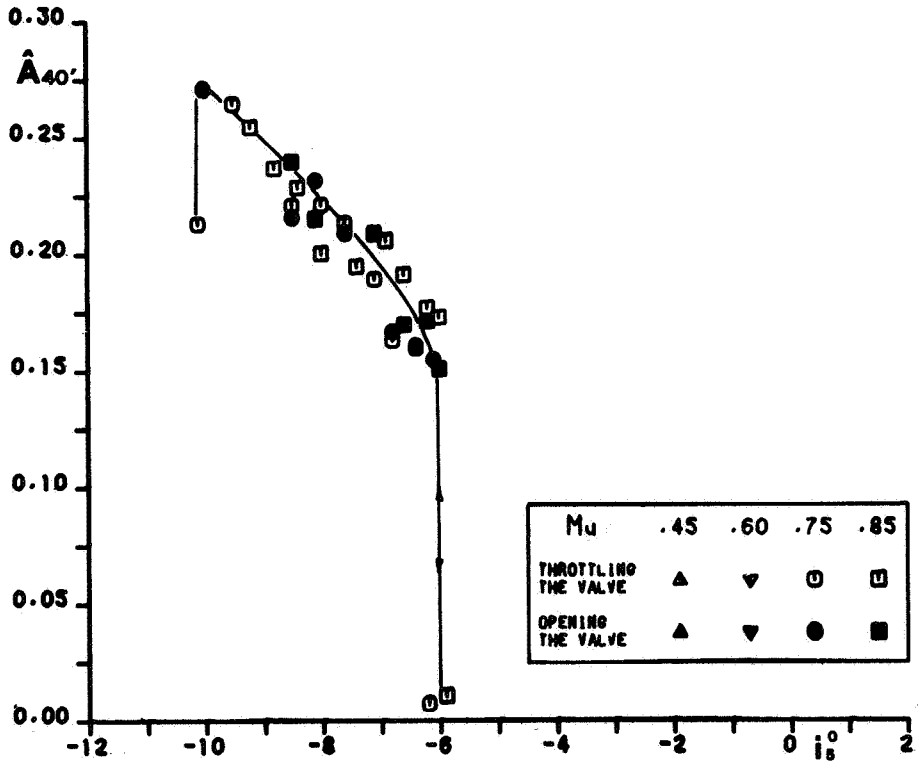

Figure 38. - Nondimensional amplitude at section 40' versus incidence angle. (Configuration A with sandpaper.)

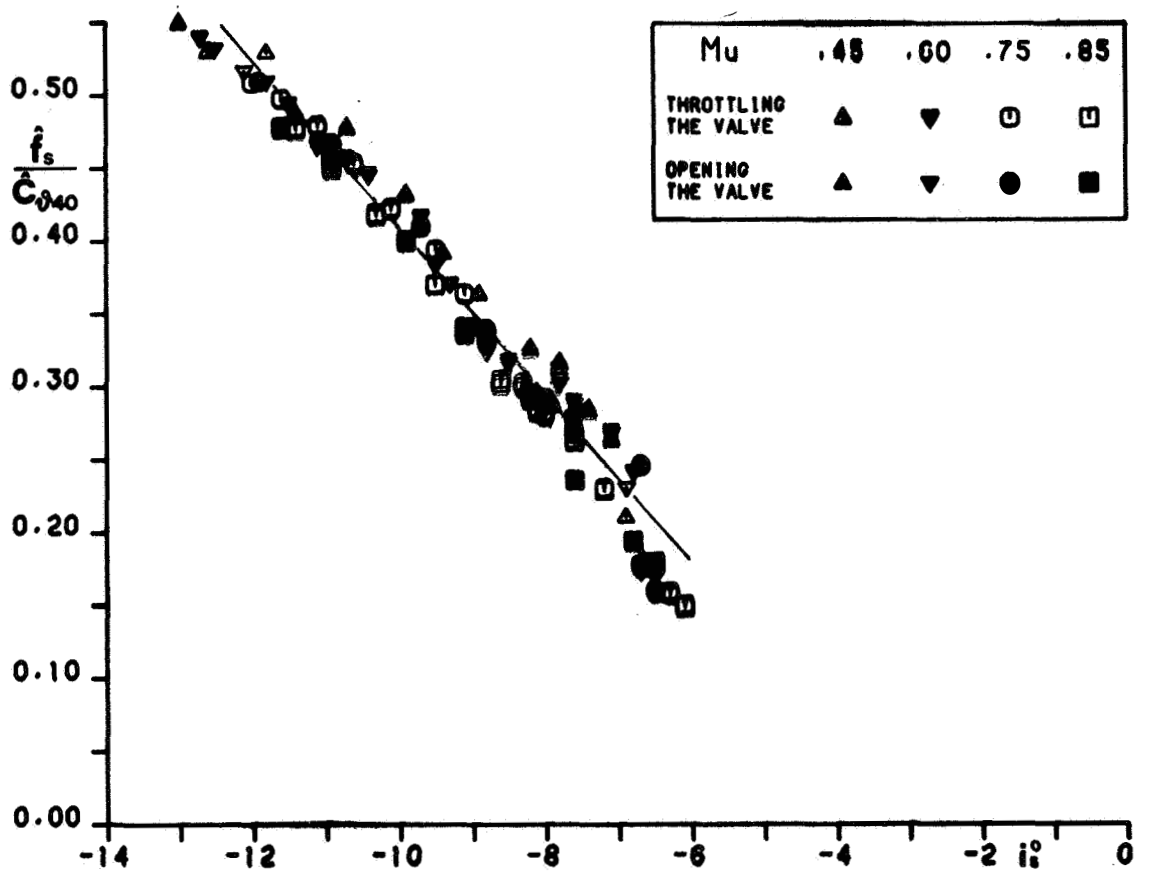

Figure 39. - Nondimensional frequency versus incidence angle. (Configuration B.)

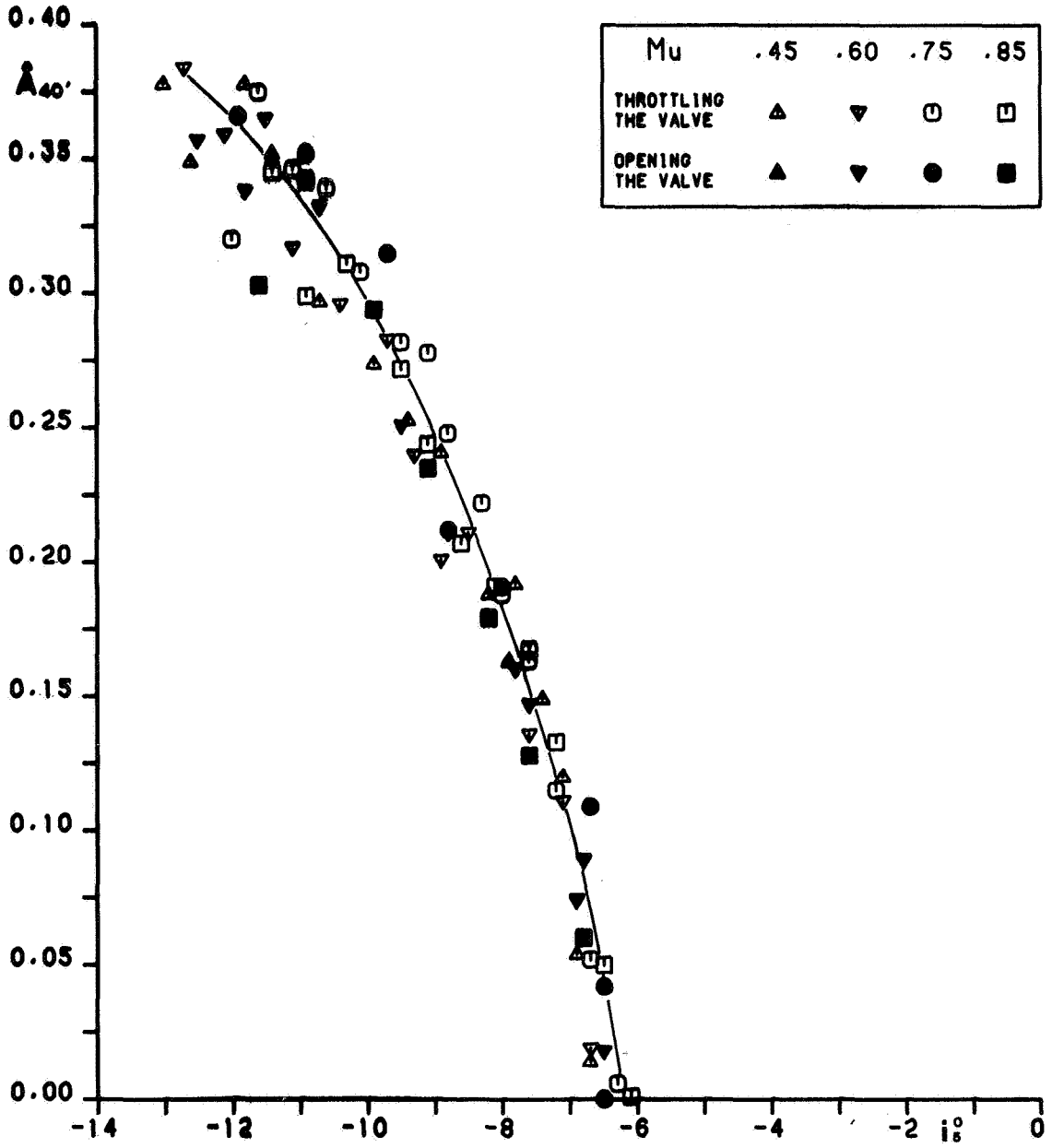

Figure 40. - Nondimensional amplitude at section 40' versus incidence angle. (Configuration B.)

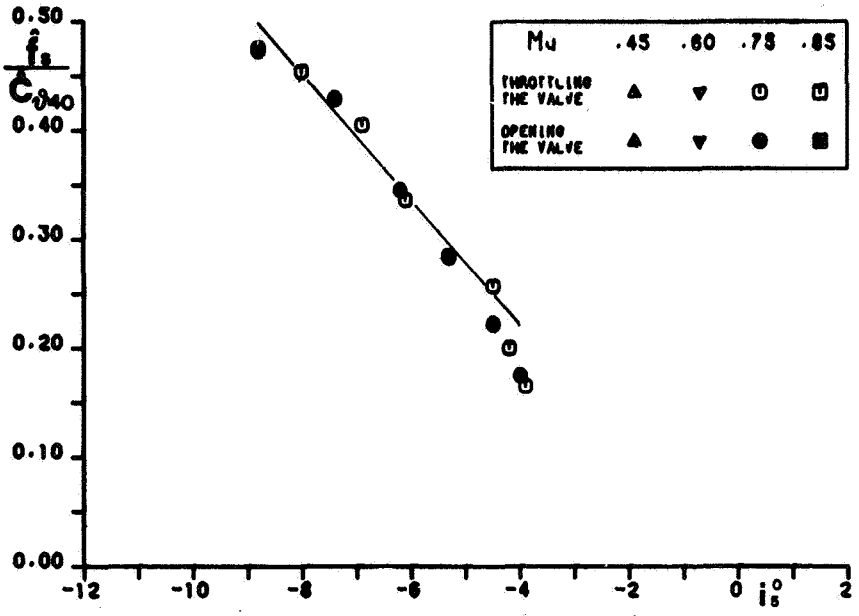

Figure 41. - Nondimensional frequency versus incidence angle. (Configuration C.)

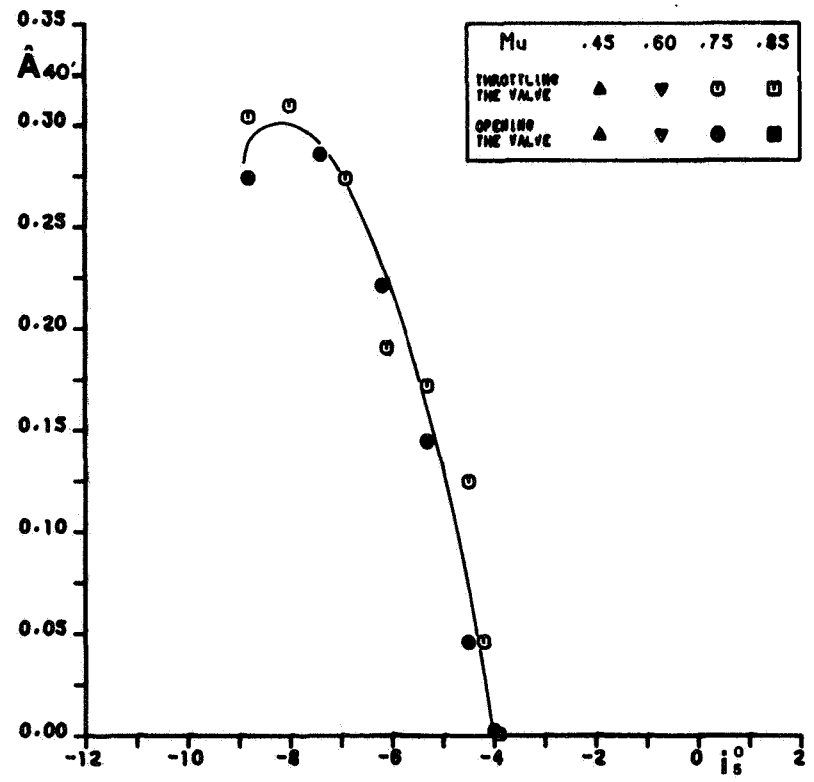

Figure 42. - Nondimensional amplitude at section 40' versus incidence angle. (Configuration C.)

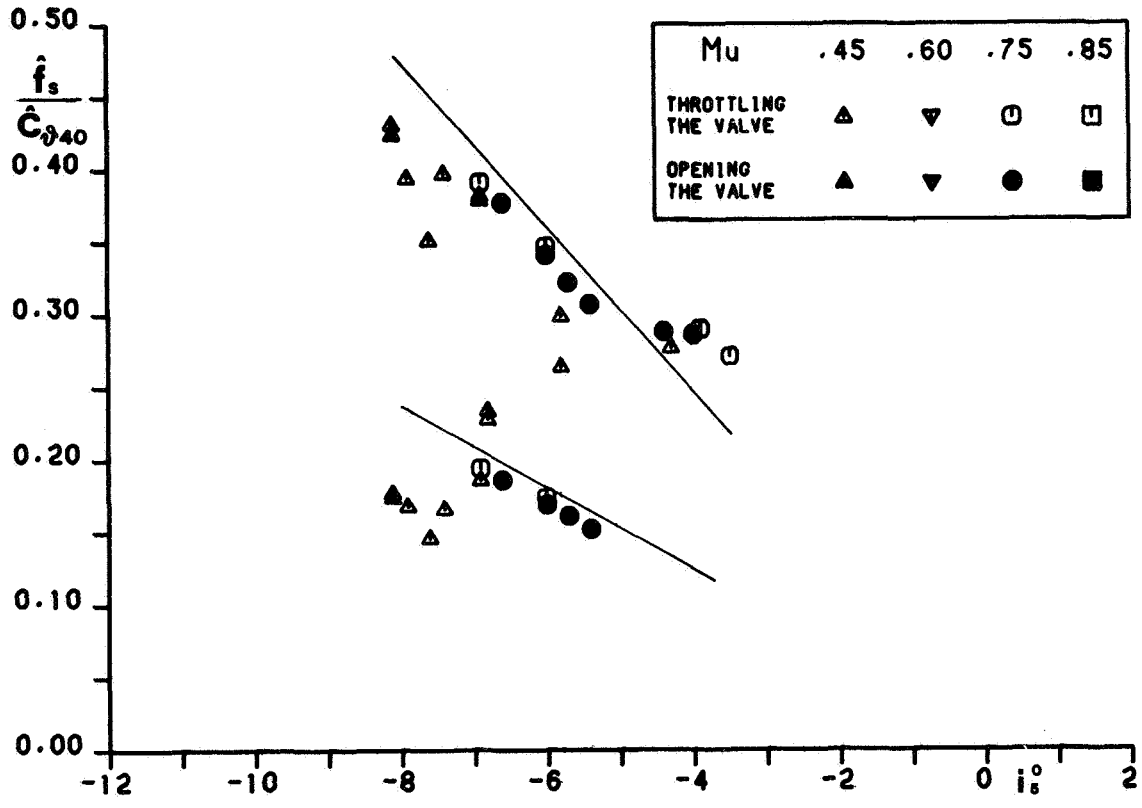

Figure 43. - Nondimensional frequency versus incidence angle. (Configuration D.)

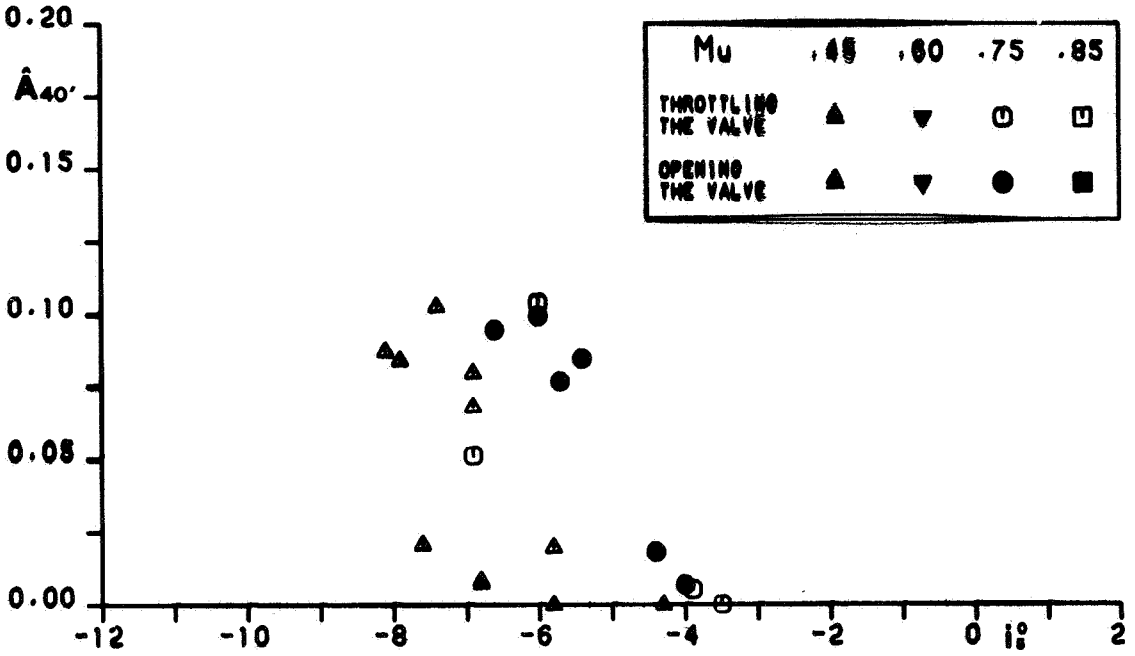

Figure 44. - Nondimensional amplitude (fs) at section 40' versus incidence angle. (Configuration D.)

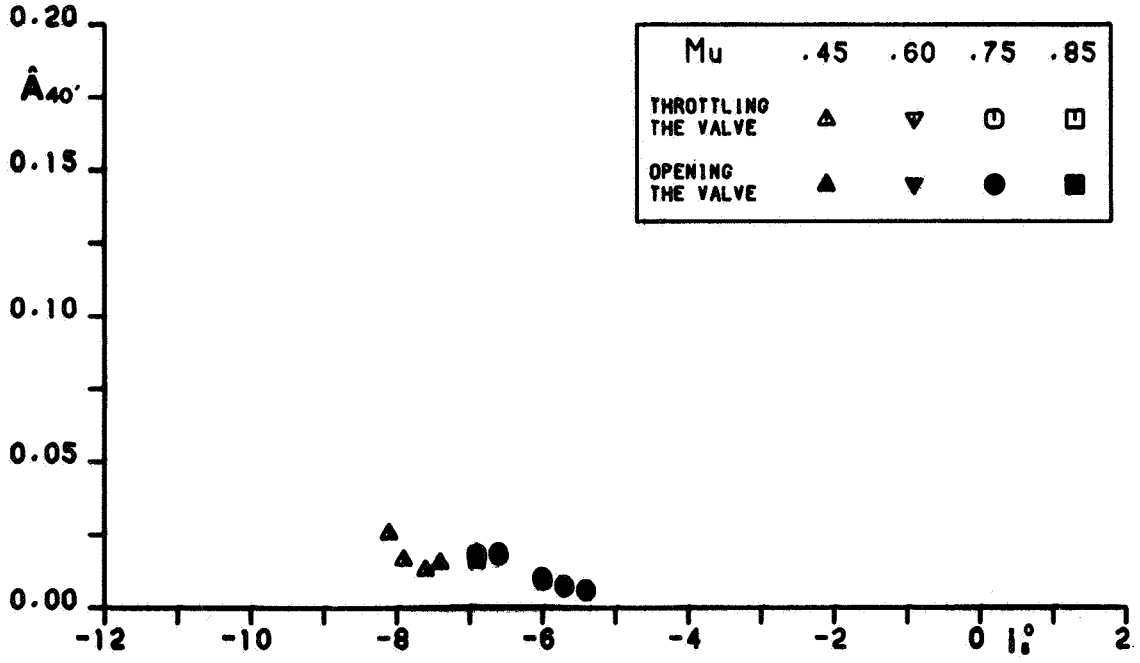

Figure 45. - Nondimensional amplitude (fs/2) at section 40' versus incidence angle. (Configuration D.)

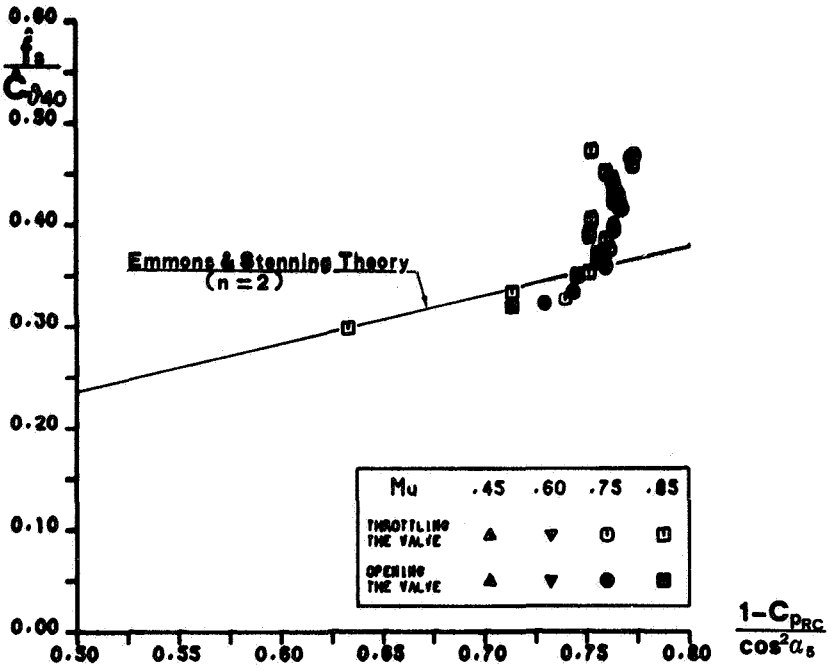

Figure 46. - Nondimensional observed frequency. (Configuration A with sandpaper.)

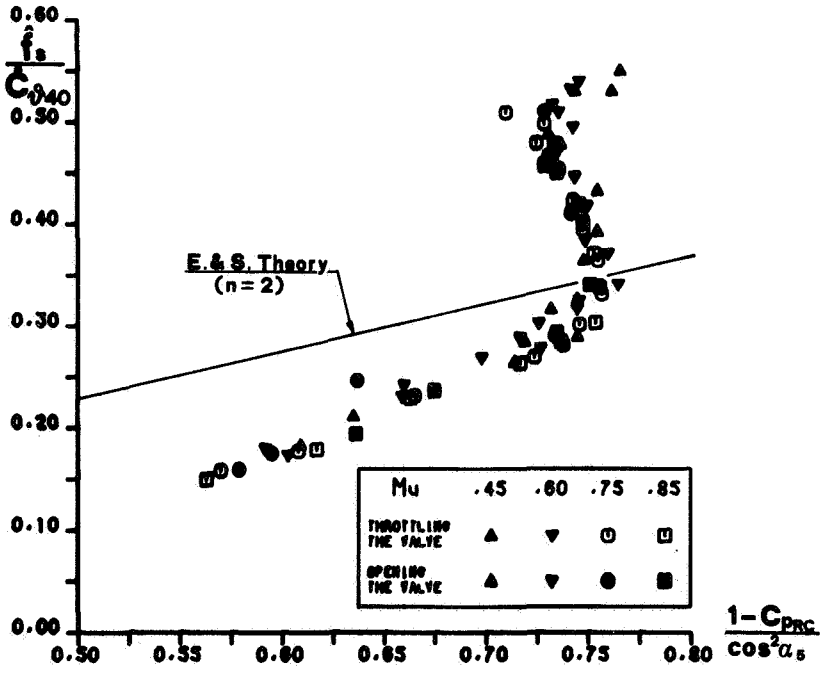

Figure 47. - Nondimensional observed frequency. (Configuration B.)

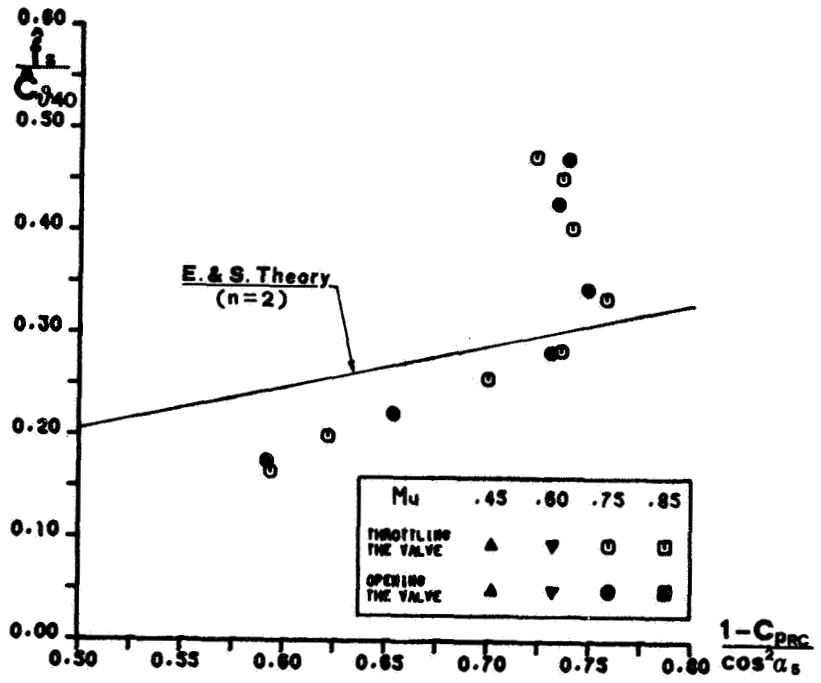

Figure 48. - Nondimensional observed frequency. (Configuration C.)

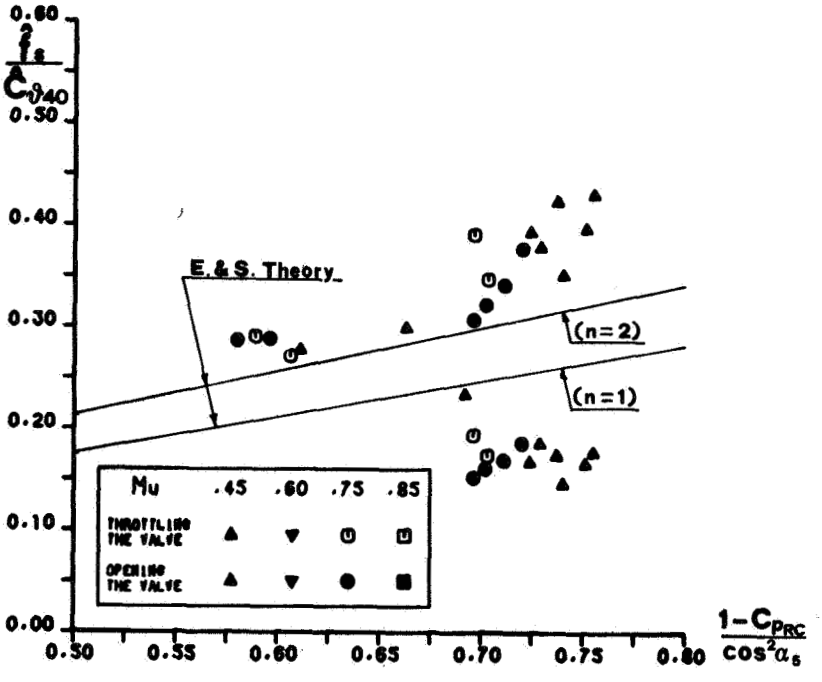

Figure 49. - Nondimensional observed frequency. (Configuration D.)